

RIS-Assisted Energy Harvesting Gains for Bistatic Backscatter Networks: Performance Analysis and RIS Phase Optimization

Diluka Galappaththige*, *Member, IEEE*, Fatemeh Rezaei*, *Member, IEEE*, Chintla Tellambura, *Fellow, IEEE*, Sanjeeva Herath, *Member, IEEE*

Abstract—Inexpensive tags powered by energy harvesting (EH) can realize green (energy-efficient) Internet of Things (IoT) networks. However, tags are vulnerable to energy insecurities, resulting in poor communication ranges, activation distances, and data rates. To overcome these challenges, we explore the use of a reconfigurable intelligent surface (RIS) for EH-based IoT networks. The RIS is deployed to enhance RF power at the tag, improving EH capabilities. We consider linear and nonlinear EH models and analyze single-tag and multi-tag scenarios. For single-tag networks, the tag’s maximum received power and the reader’s signal-to-noise ratio with the optimized RIS phase-shifts are derived. Key metrics, such as received power, harvested power, achievable rate, outage probability, bit error rate, and diversity order, are also evaluated. The impact of RIS phase shift quantization errors is also studied. For the multi-tag case, an algorithm to compute the optimal RIS phase-shifts is developed. Numerical results and simulations demonstrate significant improvements compared to the benchmarks of no-RIS case and random RIS-phase design. For instance, our optimal design with a 200-element RIS increases the activation distance by 270 % and 55 % compared to those benchmarks. In summary, RIS deployment improves the energy autonomy of tags while maintaining the basic tag design intact.

Index Terms—Bistatic backscatter communication (BiBC), Reconfigurable intelligent surface (RIS), Performance analysis.

I. INTRODUCTION

A. The Problems with Energy Harvesting Backscatter Tags

Parcel tracking using passive electronic tags is one of the many potential applications of the Internet of Things (IoT). The global parcel volume surpassed 131 billion in 2020, showing a 27 % year-over-year increase. In the United States alone, 59 million parcels were generated daily in 2021, projected to reach 25-40 billion with a 5 %-10 % annual growth rate from 2022-2027. Similar growth trends are observed globally. Barcode-based tracking is currently employed, but electronic tag-based tracking offers advantages such as enhanced labor productivity, throughput, warehousing efficiency, and real-time data accuracy for quality control. Tags without batteries are particularly suitable because of their cost-effectiveness and compact size. Their applications include medical and healthcare, agriculture, livestock, logistics, retail chains, and passive IoT networks [1]–[3]. These tags have low-cost and low-power circuits with limited processing capabilities. They

rely on backscatter modulation, a process described in detail in [4], [5], where they reflect radio-frequency (RF) signals to communicate with the reader.

Passive tags encounter two main problems related to their reliance on RF energy harvesting (EH) for power: activation failure and energy outage (EO). Activation failure occurs when the tag fails to reach the activation threshold (P_b), typically around -20 dBm [6], required to initiate the EH circuitry [7]. Imperfections in the matching network between the tag’s antenna and the EH circuit can cause this failure. The matching network aims to align the complex impedance of the EH circuit with the antenna’s impedance, optimizing power transfer and minimizing signal reflections. However, the EH circuit’s impedance depends on the incident input power due to nonlinear devices, leading to reduced circuit efficiency with changes in input power. The second problem is EO. Ambient energy sources are unpredictable with RF power density values as low as $1\sim 100\mu\text{W}/\text{cm}^2$ and varying with distance [3]. As a result, there is a risk of an EO where the tag does not reach the activation threshold. These problems cause ultra-low power (nW- μW), short communication ranges (≤ 6 m), short activation distances, and low data rates (≤ 1 bps/Hz). It is clear that all these problems are initiated whenever the incident RF energy is low. Addressing that issue is the main focus of this paper.

Backscatter networks can be categorized into three types: monostatic, bistatic, and ambient. In monostatic systems, the reader and emitter are co-located, resulting in doubled path loss [8]. Ambient systems rely on reflecting existing RF signals, which are highly unpredictable. Bistatic systems, on the other hand, offer better support for applications such as warehouses (Fig.1). These systems deploy dedicated RF emitters, either single or multiple, to provide energy to the tags and enable backscatter modulation. By optimizing the locations of multiple emitters, a larger area can be covered (Fig.1), maximizing coverage and performance. Dedicated emitters have advantages over ambient signals, including predictability, reduced interference, control over the system, and knowledge of ambient signal parameters [9]. However, the high cost, complexity, and transmit powers associated with dedicated emitters can be problematic.

These considerations motivate the following questions: 1) what is the best way to increase the chance of the incident RF power on the tag exceeding P_b ? 2) How can that goal be reached without increasing dedicated RF emitters’ cost and energy expenditure?

*D. Galappaththige and F. Rezaei contributed equally to this work.

D. Galappaththige, F. Rezaei, and C. Tellambura with the Department of Electrical and Computer Engineering, University of Alberta, Edmonton, AB, T6G 1H9, Canada (e-mail: {diluka.lg, rezaeidi, ct4}@ualberta.ca).

S. Herath is with the Huawei Canada, 303 Terry Fox Drive, Suite 400, Ottawa, Ontario K2K 3J1 (e-mail: sanjeeva.herath@huawei.com).



Fig. 1: A warehouse use case of BiBC network.

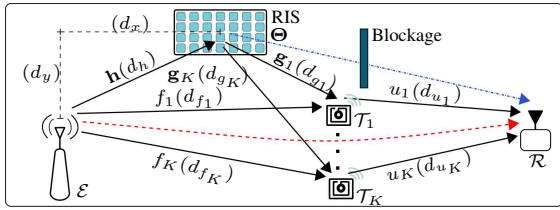


Fig. 2: An RIS-assisted BiBC. Red lines denote interference signals and d_{f_k} , d_{g_k} , d_{u_k} and d_h are respectively \mathcal{E} - \mathcal{T}_k , RIS- \mathcal{T}_k , \mathcal{T}_k - \mathcal{R} , and \mathcal{E} -RIS distances.

B. Existing Solutions

Various solutions can enhance the performance of passive tags, including the use of multi-antenna configurations [10], energy beamforming techniques, RF energy harvesters with improved activation thresholds [11], and channel coding methods [5], [12]. Additionally, active tunnel diodes in the tags have been explored as a solution [13]. However, these techniques may not be feasible for passive tags due to their limited processing capability, power constraints, and cost limitations. Increasing the transmit power at the emitter or deploying multiple emitters is also not an energy-efficient (green) solution.

To overcome these issues, study [14] is the first to propose the use of a reconfigurable intelligent surface (RIS) in BiBC networks. A RIS is a synthetic surface consisting of numerous passive reflectors, also known as meta-material elements [15], [16]. These reflectors have the ability to independently modify the characteristics of incoming electromagnetic waves, such as phase, amplitude, frequency, or polarization [15], [16]. Through real-time adaptation, the reflectors can be programmed to dynamically adjust to the wireless channel conditions. Each reflector is equipped with one or more switches, with a switching frequency of up to 5 MHz, which ensures minimal switching time compared to the channel coherence time [17]. By dynamically adjusting the reflectors, the RIS controller coordinates their actions to create constructive and destructive interference patterns in the reflected waves as required [15], [16].

A RIS consumes a few watts during the reconfiguration states and much less during idle states, e.g., 6 mW per element for 4-bits resolution phase shifting [18]. A RIS can provide significant gain even without an amplifier, ranging from 30 dB to 40 dB relative to the isotropic radiation depending on the size of the surface and frequency [15], [16]. Typically, the size

of a single reflector is much smaller than the signal wavelength (λ), ranging between $\lambda/10$ and $\lambda/5$ [16]. The RIS integrates with existing networks without modifying the basic network design [19].

C. Problem Statement and Contributions

We address the problem of maximizing the number of passive tags supported in a given area, such as a large warehouse (Fig.1) while minimizing the number of carrier emitters required. As mentioned before, passive tags have limited activation/communication ranges and data rates, relying on a minimum RF power (activation threshold) for self-activation. Existing solutions like multiple-antenna tags, coding, batteries, multiple emitters, repeaters, and relays have certain limitations. To overcome these challenges, we adopt the approach proposed in [14] by deploying a RIS in the BiBC network (Fig.2). The RIS increases the incident RF power on the tags, allowing them to harvest more energy and improving their reliability and communication range. Optimal placement and configuration of the phase shift elements in the RIS can be determined to achieve maximum gains. Moreover, continuous phase shifts (i.e., infinite levels in $[-\pi, \pi)$) are not viable because more switches per reflector will cost more for the RIS. For 16 phase shifts, $\log_2(16) = 4$ switches are needed [20]. Hence, to keep the size, cost, and power consumption of the RIS down, phase quantization is essential.

We propose using a RIS in the BiBC network (Fig. 2) to enhance its energy security and performance. Initially, we consider the case of a single tag and assume a linear energy EH model for the tag. The RIS acts as a reflector, increasing the power delivered to the passive tags by reflecting the RF emitter signal. By optimizing the phase shifts of the RIS, we aim to improve harvested power, communication range, and data rate. Our results provide insights into the improvements in harvested energy, data rate, and reliability achieved through the use of the RIS. Furthermore, to support passive IoT applications involving multiple tags, we develop RIS optimization techniques that aid tag activation while enhancing communication performance.

Our study differs from [14] in several aspects. Firstly, we focus on increasing the energy security of passive tags, resulting in improved activation distance, communication range, and data rates. In contrast, [14] primarily aims to enhance the communication performance of passive/semi-passive tags. We achieve this by employing a RIS in the source-to-tag links, which enhances the incident energy at the tags. In contrast, [14] uses a RIS to increase the signal-to-noise ratio (SNR) at the reader, serving a different purpose. Secondly, our study utilizes fully passive tags with reflective modulation schemes such as binary phase-shift keying (BPSK), implemented by switching the tag's impedance between two levels. These passive modulation schemes can be easily extended to higher-order quadrature phase-shift keying (QPSK) and M -quadrature amplitude modulation (QAM) [4], [5]. On the other hand, [14] employs semi-passive and passive tags with frequency-shift keying (FSK) modulation to enable multiple access. However, implementing FSK requires more from the

tags as they need to generate distinct carrier frequencies. Therefore, achieving higher-order FSK may not be feasible with simple tags. Thirdly, in [14], the beamformer at the multi-antenna emitter and the RIS phase shifts are optimized to minimize the transmit power at the emitter. In our study, we aim to maximize the sum rate of multiple tags by optimizing RIS phase shifts with a single-antenna emitter that maintains constant transmit power.

As well, there are analytical and algorithmic differences between our study and [14]. While [14] uses a minorization maximization (MM) algorithm with a semi-passive tag, we propose a closed-form solution for RIS phase shifts that simultaneously maximize the received power of the passive tag and the SNR at the reader. This analytical framework allows us to quantify the benefits of utilizing an RIS for a single passive tag. We evaluate system efficiency, reliability, and error performance through metrics such as harvested power, achievable rate, outage probability, bit error rate (BER), achievable diversity order, and RIS phase shift quantization errors. Additionally, in the multi-tag scenario, [14] extends the single-tag MM algorithm with minor modifications. In contrast, we employ a fractional programming-based optimization approach that enables multiple access for passive tags. Our approach focuses on maximizing the sum rate of the tags while ensuring tag activation and reducing tag-to-tag interference.

Specifically, the main contributions of this paper can be summarized as follows:

- 1) In the single-tag network, we optimize the RIS phase shifts to maximize the received signal power at the tag. This has a closed-form solution, allowing us to determine the optimal RIS phase shifts directly. Furthermore, we analyze the impact of the RIS on the EH process by deriving the average harvested power at the tag. This quantifies the role of the RIS in enhancing the EH performance.
- 2) To analyze the performance of the system, we require the probability density function (PDF) and cumulative distribution function (CDF) of the optimal SNR at the reader. However, obtaining analytical expressions for these functions appears intractable, even in the single-tag case. To overcome this challenge, we test Gaussian and Gamma approximations for the PDF and CDF by assuming a Nakagami- m fading. Among the two approximations, we select the Gamma approximation as it provides a more accurate analysis of the harvested power, achievable rate, outage probability, BER, and achievable diversity order.
- 3) We also investigate the effect of RIS phase shift errors to quantify the effects of hardware limitations and imperfect channel estimation in practical scenarios.
- 4) We further explore the optimization of the RIS for a multi-tag scenario. To this end, we introduce an iterative algorithm that aims to maximize the achievable sum rate while ensuring that each tag meets its minimum power requirement. This goal is achieved by optimizing the RIS phase shifts iteratively.
- 5) Our simulations and numerical results validate the accuracy of the derived analytical results, demonstrating a

close agreement between them. These simulations provide valuable insights for system design and assessment, aiding in the practical implementation and evaluation of the proposed approach.

We show that RIS optimization provides a green solution for energizing and improving the activation distance and communication range of passive tags, enabling massive connectivity without modifications or additional processing at the tag. This makes passive tags suitable for forming the backbone of passive IoT networks. The analytical results presented in this paper offer valuable insights for practical applications. Before proceeding to the technical contributions, we provide an overview of related works in the field of RIS-assisted BackCom literature.

D. Previous Contributions on RIS-Assisted BackCom

Existing works often overlook the tag activation requirement and primarily concentrate on utilizing RIS to enhance the tag-reflected signal for improved communication. However, this approach assumes either the use of active tags powered by batteries, where energy harvesting is unnecessary, or tags that can be activated with extremely low power ($P_b = -\infty$), which is not representative of actual tags. These works optimize the RIS without considering the EH constraint, aiming to improve outage, sum rates, error probabilities, or other metrics. References [21]–[28] fall into this category and differ significantly from our contribution. A summary of relevant and recent contributions is provided in Table I.

In contrast to the works [21]–[28], a few studies [14], [29], [30] have explored the use of RIS to enhance the EH potential of backscatter networks. In [14], RIS was applied to a BiBC network, serving as the inspiration for our study. The main purpose of the RIS in [14] was to improve the signal-to-noise ratio (SNR) at the reader. In contrast, we utilize the RIS to enhance the RF signal received by the tags. Earlier, we discussed the differences between [14] and our study.

Another study [29] utilizes a RIS to enable direct tag-to-tag communication when the direct source-to-tag links are blocked. If the tag receives signal power exceeding a certain threshold P_b , it first harvests energy and then reflects its data. Otherwise, it operates using a battery. Hence, [29] considers the use of semi-passive tags, which is fundamentally different from ours. In our previous work [30], we also explored the use of a RIS to energize a single tag in an AmBC network, where the RIS is optimized to satisfy the tag's EH constraint while minimizing interference from the ambient source. Once again, the system model in that study is distinct from the one considered here.

Structure: This paper is structured as follows. Section II introduces the system and channel model, including the tag and signal models. The analysis of the single-tag system is presented in Section III. Section IV explores the multi-tag scenario. The analytical results are validated through simulation examples in Section V. Finally, Section VI provides the conclusion of the paper and outlines potential future research directions.

Notation: For random variable X , $f_X(\cdot)$ and $F_X(\cdot)$ denote PDF and CDF. $\mathbb{E}\{\cdot\}$ and $\text{Var}\{\cdot\}$ denote the expectation and

TABLE I: Summary of related works.

Setup	Reference	Tag type	EH constraint	Contribution
MoBC	[21]	–	✗	BER analysis
	[22]	–	✗	BER, outage, and rate analysis
	[23]	Passive	✗	BER and coverage analysis
AmBC	[24]	–	✗	BER analysis
	[29]	Passive/Semi-passive	✓	Throughput and coverage analysis
	[25]	Semi-passive	✗	Outage and spectral efficiency analysis
	[26]	Passive	✗	Outage and BER analysis
	[30]	Passive	✓	Rate maximization
	[28]*	–	✗	Transmit power minimization
	[27]	–	✗	Rate maximization
BiBC	[14]	Semi-passive/Passive	✓	Transmit power minimization
	This Paper	Passive	✓	BER, outage, rate, and harvested power analysis Rate maximization

* Symbiotic radio - the reader supports both the primary and the backscatter transmission

variance. Lowercase bold and uppercase bold denote vectors and matrices. \mathbf{A}^T , \mathbf{A}^H denote transpose and Hermitian transpose of matrix \mathbf{A} . Moreover, the positive part of real x is denoted by $[x]^+ = \max(0, x)$. The gamma function $\Gamma(a)$ is given in [31, Eq. (8.310.1)], $D_\nu(x)$ is parabolic cylinder function [31, eq. (9.240)], and $\gamma(n, x)$ is the lower incomplete gamma function [31, Eq. (8.350)]. The complementary error function is $\text{erfc}(x)$ [31, eq. (8.25.4)] and $Q(x) = \frac{1}{2}\text{erfc}(x/\sqrt{2})$ is the Gaussian Q -function. Finally, $\mathcal{CN}(\boldsymbol{\mu}, \mathbf{R})$ is a complex Gaussian vector with mean $\boldsymbol{\mu}$ and co-variance matrix \mathbf{R} .

II. SYSTEM MODEL AND PRELIMINARIES

A. System and Channel Models

We consider a RIS-assisted BiBC setup consisting of a single-antenna emitter (\mathcal{E}), K -single-antenna passive tags, a single-antenna reader (\mathcal{R}), and a RIS with N passive reflective elements (Fig. 2). We use \mathcal{T}_k to denote the k th tag. Since tags are batteryless and entirely rely on EH, we deploy a RIS to deliver as much RF power as possible. To do this, the RIS controller sets the states of individual reflectors to adjust the phase shifts intelligently to maximize the received power at each tag. For this, the controller requires channel state information (CSI) for all the channels in Fig. 2. We assume that the controller has a backhaul connection between the RIS and \mathcal{E} , which can provide all such necessary information [32]. For brevity, we index the set of RIS passive elements as $\mathcal{N} = \{1, \dots, N\}$ and the set of tags as $\mathcal{K} = \{1, \dots, K\}$.

We consider a block, flat-fading channel model where the channel response remains constant over the duration of a block and changes independently from block to block [33]. During each fading block, the direct channel coefficients in the \mathcal{E} - \mathcal{T}_k link and the \mathcal{T}_k - \mathcal{R} link are denoted as f_k and u_k , respectively. Moreover, the channel coefficient vectors in the \mathcal{E} -RIS link and the RIS- \mathcal{T}_k link are denoted as $\mathbf{g}_k = [g_{k,1}, \dots, g_{k,N}]^T \in \mathbb{C}^{N \times 1}$ and $\mathbf{h} = [h_1, \dots, h_N]^T \in \mathbb{C}^{N \times 1}$, respectively. Here, $g_{k,n}$ and h_n for $n \in \mathcal{N}$ and $k \in \mathcal{K}$ are the channels between the n th element of the RIS and \mathcal{T}_k , and the n th element of the RIS and \mathcal{E} , respectively. All channel envelopes are assumed to be independent Nakagami- m distributed, where m is the shape

parameter [34]. A unified representation of all four channels $\mathcal{A} = \{f_k, u_k, h_n, g_{k,n}\}$ is thus given as

$$a = \alpha_a \exp(j\theta_a), \quad (1)$$

where α_a is the envelope of the a and $\theta_a \in [-\pi, \pi]$ is the phase of a . The PDF of α_a is given as

$$f_{\alpha_a}(x) = \frac{2m_a^{m_a} x^{2m_a-1}}{\Gamma(m_a)\Omega_a^{m_a}} \exp\left(\frac{-m_a x^2}{\Omega_a}\right), \quad (2)$$

where m_a is the shape parameter and $\Omega_a = m_a \zeta_a$ is the scaling parameter, in which ζ_a accounts for the large-scale fading/path-loss. It should be noted that, since the RIS reflective elements are co-located, the large-scale fading parameters are the same for all of them, i.e., $\zeta_{g_{k,n}} = \zeta_{g_k}$ and $\zeta_{h_n} = \zeta_h$ for $n \in \mathcal{N}$.

Remark 1. *The Nakagami- m model is versatile to represent a variety of propagation environments. For instance, $m = 1$ represents Rayleigh fading, and $m \rightarrow \infty$ represents the no fading scenario. Hence, our performance analysis covers the special case of Rayleigh fading channels [21], [35].*

We make the following key assumptions:

- A1: Perfect channel state information (CSI) is available for the \mathcal{E} - \mathcal{T}_k , \mathcal{E} -RIS, RIS- \mathcal{T}_k , \mathcal{T}_k - \mathcal{R} , and \mathcal{E} - \mathcal{R} channels in the system. However, channel estimation poses challenges due to the passive nature of the RIS and tags, as well as the large number of RIS elements. Sophisticated methods and novel pilot designs are required for accurate estimation. While a comprehensive treatment of channel estimation is beyond the scope of this work, a possible estimation strategy for the system in Fig. 2 can be envisioned. Initially, the RIS is set to the non-reflecting state, allowing estimation of the direct \mathcal{E} - \mathcal{R} link, the \mathcal{E} - \mathcal{T}_k - \mathcal{R} link, and the \mathcal{E} - \mathcal{T}_k link using existing methods [36], [37]. Subsequently, the cascaded \mathcal{E} -RIS- \mathcal{R} channel can be resolved into its \mathcal{E} -RIS and RIS- \mathcal{R} components using appropriate techniques [38]. Finally, the RIS- \mathcal{T}_k channels can be obtained using information from other available paths. Thus, this assumption is justified because emerging techniques can address the challenges associated with channel estimation.
- A2: We assume that the RIS- \mathcal{R} link (blue line in Fig. 2) is blocked or negligible because the RIS focuses the

reflected beam toward the tags [39]. The \mathcal{E} - \mathcal{R} signal (red line in Fig. 2) is interference felt at \mathcal{R} . When \mathcal{R} has CSI and knows the signal of \mathcal{E} , it can cancel this interference signal [14], [40], [41]. If full CSI is unavailable or cancellation is impossible, our analytical results serve as fundamental limits or upper bounds of achievable performance.

A3: We consider the linear model for the EH process at \mathcal{T}_k . Even though practical EH circuits have non-linear operating characteristics and an activation threshold, the linear model can be accurate in certain operating regions.

B. Passive Tag Operation

As mentioned before, we consider the use of passive tags only as they have the potential to enable massive connectivity at a low cost. Thus, \mathcal{T}_k does not have batteries and entirely relies on the harvested energy from the RF signal transmitted by \mathcal{E} . Specifically, the harvested energy powers \mathcal{T}_k 's circuit operation and enables it to backscatter data to \mathcal{R} simultaneously [42]. Thus, the amount of harvested energy is the fundamental parameter that ensures the success or failure of \mathcal{T}_k to communicate. We next set up the basics necessary to estimate the EH ability of \mathcal{T}_k .

Let $P_{T,k}$ be the received power at \mathcal{T}_k 's antenna. The reflection coefficient of \mathcal{T}_k is then given as $\sqrt{\beta}q_m$, where q_m is the normalized backscatter symbol selected from a multi-level (M -ary) modulation (i.e., $|q_m|^2 \leq 1$) and $0 < \beta < 1$ is the fraction of power reflected at \mathcal{T}_k . Therefore, when \mathcal{T}_k reflects the RF signal, $\beta P_{T,k}$ of the RF power is reflected while the rest $P_{l,k} = (1 - \beta)P_{T,k}$ is absorbed for EH purposes. The EH circuits convert the RF power $P_{l,k}$ into direct current (DC) power by using a rectifier. With linear and nonlinear models for the energy harvester, the harvested DC power ($P_{h,k}$) can be defined as [7]

$$P_{h,k} = \begin{cases} \phi P_{l,k}, & \text{Linear,} \\ \Phi(P_{l,k}), & \text{Nonlinear,} \end{cases} \quad (3)$$

where ϕ is the power conversion efficiency, typically measured around 31.8% to 61.4% at 2.45 GHz [43], independent of the RF power $P_{l,k}$. Moreover, $\Phi(\cdot)$ represents the nonlinear EH function [7]. Although the linear model offers simplicity, non-linear EH models are also widely used (see [7], [44] and references therein). However, our solution can be easily extended to such models as well. We omit the details for brevity.

C. Signal Model

Node \mathcal{E} transmits an unmodulated carrier signal $\sqrt{P}s$ to energize tags, where s is the carrier signal satisfying $\mathbb{E}\{|s|^2\} = 1$ and P is the carrier transmission power. In general, s should be designed to maximize the EH potential of tags. Thus, waveforms with high peak-to-average power ratio (PAPR) are used as these increase the RF-to-DC conversion efficiency of the tag's EH circuit [45]. Hence, s can be white noise, with a flat power spectral density and high PAPR [46]. Other designs include orthogonal frequency-division multiplexing (OFDM), chaotic, and multisine waveforms [45], [46].

The signal $\sqrt{P}s$ is received at \mathcal{T}_k through the direct channel, f_k , and the reflective channels of the RIS, \mathbf{h} and \mathbf{g}_k . The received signal at \mathcal{T}_k is thus given as¹

$$y_k = \sqrt{P}f_k s + \sqrt{P}\mathbf{g}_k^T \Theta \mathbf{h} s. \quad (4)$$

The first term is due to the direct path and the second is from the RIS's reflective elements. In (4), $\Theta \in \mathbb{C}^{N \times N}$ is a diagonal matrix that captures the reflection properties (the magnitude of attenuation and the phase shift) of the RIS elements, i.e., $\Theta = \text{diag}(\eta_1 \exp(j\theta_1), \dots, \eta_N \exp(j\theta_N))$, where $\eta_n \exp(j\theta_n)$ is the reflection coefficient of the n -th RIS element with the magnitude of attenuation η_n and the phase shift $\theta_n \in [-\pi, \pi]$. Discrete phase shifts, resulting in a phase quantization error, will be treated in Section III-H. Moreover, here we only consider a passive RIS without active amplification, i.e., $\eta_k \leq 1, \forall k$. However, an active RIS that can amplify and reflect incident RF signals, i.e., $\eta_n > 1$, is a potential future extension of this work.

Using (4), the received power at \mathcal{T}_k is given as

$$P_{T,k} = P|f_k + \mathbf{g}_k^T \Theta \mathbf{h}|^2. \quad (5)$$

\mathcal{T}_k harvests energy from the received power, $P_{T,k}$ (5), and modulates the received signal with its normalized M -ary backscatter signal, q_k , $\mathbb{E}\{|q_k|^2\} = 1$, to be transmitted to \mathcal{R} . The received signal at \mathcal{R} is thus given as

$$y_R = \sqrt{\beta P} \sum_{k \in \mathcal{K}} u_k (f_k + \mathbf{g}_k^T \Theta \mathbf{h}) s q_k + z, \quad (6)$$

where $z \sim \mathcal{CN}(0, \sigma_z^2)$ is additive white Gaussian noise (AWGN) with mean 0 and variance σ_z^2 .

III. SINGLE-TAG SYSTEM

Here, we consider $K = 1$, i.e., the single-tag setup. The RIS phase shifts should be optimized to maximize both the received signal power at \mathcal{T} and the achievable rate at \mathcal{R} . To this end, the optimization problem is formulated as follows:

$$\mathcal{P}_{S,1} : \underset{\Theta}{\text{maximize}} \quad \log_2(1 + \gamma), \quad (7a)$$

$$\text{subject to} \quad (1 - \beta)P_T \geq P'_b, \quad (7b)$$

$$|\bar{\theta}_n| \leq 1, \quad (7c)$$

where $\bar{\theta}_n = \eta_n \exp(j\theta_n)$ and $P'_b \triangleq P_b/\phi$ is the respective threshold value. Note that this constraint is equivalent to the nonlinear EH case with $P'_b = \Phi^{-1}(P_b)$. Hence, we adopt the linear EH model (3) due to its tractability. Here, P_T is the received signal power at \mathcal{T} and given as

$$P_T = P \left| \left(\alpha_f e^{j\theta_f} + \sum_{n \in \mathcal{N}} \eta_n \alpha_{g_n} \alpha_{h_n} e^{j(\theta_{g_n} + \theta_{h_n} + \theta_n)} \right) \right|^2. \quad (8)$$

When the tag reflects this power level, the corresponding received SNR at \mathcal{R} is given as

$$\begin{aligned} \gamma &= \bar{\gamma} |u(f + \mathbf{g}^T \Theta \mathbf{h})|^2 \\ &= \bar{\gamma} \left| \alpha_u e^{j\theta_u} \left(\alpha_f e^{j\theta_f} + \sum_{n \in \mathcal{N}} \eta_n \alpha_{g_n} \alpha_{h_n} e^{j(\theta_{g_n} + \theta_{h_n} + \theta_n)} \right) \right|^2, \end{aligned} \quad (9)$$

where $\bar{\gamma} = P\beta/\sigma_z^2$.

¹Note that, since \mathcal{T}_k is a passive device without active RF components, the noise contributed by \mathcal{T}_k can be neglected [47].

A. Proposed Solution

To maximize the received power at \mathcal{T} (which will also maximize the received SNR at \mathcal{R} if the interference is negligible), the received signal at \mathcal{T} through the RIS (the signal terms inside the summation of (8)), should be constructively added to the signal received from the direct path f , by compensating the phase distortion effect of the multipath channel, i.e., in (8), $\theta_f = \theta_{g_n} + \theta_{h_n} + \theta_n$. Thus, the phase shift at the n th RIS element should be adjusted as [32]

$$\theta_n^* = \max_{-\pi \leq \theta_n \leq \pi} P_T = \theta_f - (\theta_{g_n} + \theta_{h_n}), \quad n \in \mathcal{N}. \quad (10)$$

Thereby, the optimal received power at \mathcal{T} is derived as

$$P_T^* = P \left| \alpha_f + \sum_{n \in \mathcal{N}} \eta_n \alpha_{g_n} \alpha_{h_n} \right|^2. \quad (11)$$

Similarly, by using (10), the optimal received SNR at \mathcal{R} is derived as

$$\gamma^* = \bar{\gamma} \left| \alpha_u \left(\alpha_f + \sum_{n \in \mathcal{N}} \eta_n \alpha_{g_n} \alpha_{h_n} \right) \right|^2. \quad (12)$$

Next, we derive the approximate distributions of the optimal received power (11) and SNR (12) for the single-tag system. We develop Gaussian and Gamma approximations and compare them briefly, ultimately selecting the Gamma approximation for further analysis. Using it, we analyze various aspects of the single-tag system, including harvested power, achievable rate, outage probability, bit error rate (BER), and diversity order. Additionally, we investigate the impact of phase quantization error on the achievable rate.

B. Average Harvested Power

We first analyze the impact of the EH process before proceeding to the performance analysis section. As mentioned before, \mathcal{T} activation depends on the amount of harvested power, i.e., the sensitivity threshold, P_b , which is about -20 dBm for commercial passive RFID tags [6]. If \mathcal{T} cannot exceed this threshold, it will not be operational to reflect the RF signal to communicate its data. Thus, we can envision an EO, which will cripple the system. To understand this scenario, we will analytically determine the average harvested power below. Note that this derivation is limited to the linear EH model only because of its simplicity. However, the achievable rate, outage, and BER depend on the amount of reflected power at \mathcal{T} and hence the reflection coefficient, α .

The instantaneous harvested power at \mathcal{T} is given as $P_h = \phi(1 - \beta)P_T^*$, where ϕ is in (3) and P_T^* is the received power at \mathcal{T} (11). The average harvested power is given as

$$\bar{P}_h = \phi(1 - \beta)\mathbb{E}\{P_T^*\}. \quad (13)$$

To derive $\mathbb{E}\{P_T^*\}$, first, we define $X \triangleq \sum_{n \in \mathcal{N}} \eta_n \alpha_{g_n} \alpha_{h_n}$ and then, $\mathbb{E}\{P_T^*\}$ is given as

$$\mathbb{E}\{P_T^*\} = P \left(\sigma_{\alpha_f}^2 + \mu_{\alpha_f}^2 + \sigma_X^2 + \mu_X^2 + 2\mu_{\alpha_f}\mu_X \right), \quad (14)$$

where μ_X and σ_X^2 are respectively given as

$$\mu_X = \sum_{n \in \mathcal{N}} \eta_n \mu_{\alpha_{g_n}} \mu_{\alpha_{h_n}}, \quad (15a)$$

$$\sigma_X^2 = \sum_{n \in \mathcal{N}} \left(\mu_{x_n}^{(2)} - \mu_{x_n}^2 \right), \quad (15b)$$

in which $\mu_{x_n}^{(2)} = \eta_n^2 \mu_{\alpha_{g_n}}^{(2)} \mu_{\alpha_{h_n}}^{(2)}$, $\mu_{x_n} = \eta_n \mu_{\alpha_{g_n}} \mu_{\alpha_{h_n}}$, and

$$\mu_{\alpha_a}^{(m)} = \frac{\Gamma(m_a + \frac{m}{2})}{\Gamma(m_a)} \left(\frac{\Omega_a}{m_a} \right)^{\frac{m}{2}}, \quad (16a)$$

$$\sigma_{\alpha_a}^2 = \Omega_a \left(1 - \frac{1}{m_a} \left(\frac{\Gamma(m_a + \frac{1}{2})}{\Gamma(m_a)} \right)^2 \right), \quad (16b)$$

for $a \in \mathcal{A}$. Besides, $\mu_V = \mathbb{E}\{V\}$, $\sigma_V^2 = \text{Var}\{V\}$ and $\mu_V^{(m)} = \mathbb{E}\{V^m\}$.

C. Statistics of the Optimal Received Power and SNR

To derive the distribution of the optimal SNR (12), we consider $\gamma^* = \bar{\gamma}\Lambda^2$, where $\Lambda \triangleq \alpha_u Y$ and $Y \triangleq \alpha_f + X$. The $\alpha_u, \alpha_f, \alpha_{h_n}$, and $\alpha_{g_n}, \forall n$ are independent Nakagami- m variables, and the exact derivations of the PDFs of Y, Λ, P_T^* , and γ^* are analytically intractable. To overcome this challenge, we will develop two approximations, i.e., Gaussian and Gamma, of Y and Λ to derive the approximate distribution of P_T^* and γ^* . We will verify these via simulations.

Theorem 1. Gaussian Approximation: *Using the moment matching technique, Y and Λ can be approximated as Gaussian variables with $Y \sim \mathcal{N}(\mu_Y, \sigma_Y^2)$ and $\Lambda \sim \mathcal{N}(\mu_\Lambda, \sigma_\Lambda^2)$, within the interval $[0, \infty)$, where $\mu_Y = \mu_{\alpha_f} + \mu_X$, $\sigma_Y^2 = \sigma_{\alpha_f}^2 + \sigma_X^2$, and $\mu_\Lambda = \mu_{\alpha_u}\mu_Y$, $\sigma_\Lambda^2 = \mu_{\alpha_u}^{(2)}\mu_Y^{(2)} - \mu_Y^2\mu_{\alpha_u}^2$.*

Proof. See Appendix A. ■

Theorem 2. Gamma Approximation: *Y and Λ can be approximated as Gamma variables with $Y \sim \Gamma(k_Y, \lambda_Y)$ and $\Lambda \sim \Gamma(k_\Lambda, \lambda_\Lambda)$, where $k_C = \mu_C^2/\sigma_C^2$ and $\lambda_C = \sigma_C^2/\mu_C$ for $C \in \{Y, \Lambda\}$ are the first and second moments [48], [49]. Hence, the CDF and PDF of Y and Λ are given as*

$$F_C(r) = \frac{1}{\Gamma(k_C)} \gamma(k_C, \frac{r}{\lambda_C}), \quad (17a)$$

$$f_C(r) = \frac{1}{\Gamma(k_C)\lambda_C^{k_C}} r^{k_C-1} \exp\left(-\frac{r}{\lambda_C}\right), \quad (17b)$$

for $r \geq 0$.

Since $P_T^* = PY^2$ and $\gamma^* = \bar{\gamma}\Lambda^2$, we have

$$F_D(r) = F_d(\sqrt{r/\bar{d}}), \quad (18a)$$

$$f_D(r) = \frac{1}{(2\sqrt{\bar{d}r})} f_d(\sqrt{r/\bar{d}}). \quad (18b)$$

Here, for $D = P_T^*$, $d = Y$ and $\bar{d} = P$, and for $D = \gamma^*$, $d = \Lambda$ and $\bar{d} = \bar{\gamma}$.

Remark 2. *For Rayleigh fading channels, i.e., $m_a = 1, a \in \mathcal{A}$, $\mu_{\alpha_a} = \sqrt{\pi\Omega_a}/2$, $\mu_{\alpha_a}^{(2)} = \Omega_a$, and $\sigma_{\alpha_a}^2 = \Omega_a(4 - \pi)/4$ (16a). Besides, for $\eta_n = \eta$, $\mu_X = \pi/4N\eta\sqrt{\Omega_g\Omega_h}$, $\sigma_X^2 = (1 - (\pi/4)^2)N\eta^2\Omega_g\Omega_h$, and μ_Λ and σ_Λ^2 can be found accordingly as*

$$\mu_\Lambda = \frac{\pi}{4}\sqrt{\Omega_u\Omega_f} + \frac{\pi^{3/2}}{8}N\eta\sqrt{\Omega_g\Omega_h\Omega_u}, \quad (19a)$$

$$\sigma_\Lambda^2 = \Omega_u\sigma_Y^2 + \frac{(4 - \pi)}{4}\Omega_u\mu_Y^2, \quad (19b)$$

where $\mu_Y = \sqrt{\pi\Omega_f}/2 + \mu_X$ and $\sigma_Y^2 = \Omega_f(4 - \pi)/4 + \sigma_X^2$.

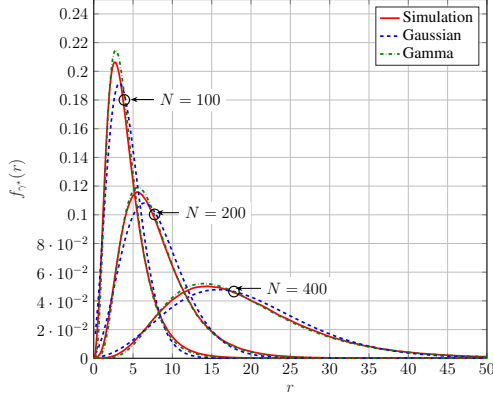


Fig. 3: The PDF of γ^* for $N = \{100, 200, 400\}$, $P = 10$ dBm, $d_f = 10$ m, $d_u = 5$ m, $d_h = 5$ m, $d_g = 6$ m, $m_f = 3$, $m_u = 5$, $m_h = 3$, $m_g = 4$, $\beta = 0.6$, and $\eta_n = 0.8$, $\forall n$.

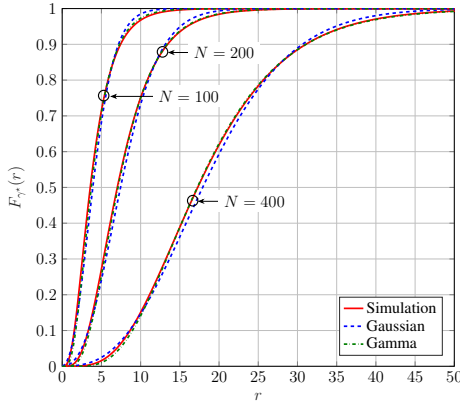


Fig. 4: The CDF of EO at \mathcal{T} as a function of d_f for $P = 20$ dBm, $d_u = 5$ m, $d_h = 1$ m, $d_g = \sqrt{d_h^2 + d_f^2}$, $m_f = m_u = m_h = m_g = 3$, $\beta = 0.6$, $\phi = 0.8$, and $\eta_n = 0.8$, $\forall n$.

To verify these approximations, we plot the PDF of γ^* in Fig. 3 for different RIS sizes, N . The Gamma approximation demonstrates better agreement with the exact simulation compared to the Gaussian approximation. As a result, we exclusively utilize it due to its superior accuracy.

Remark 3. Fig. 4 plots the CDF of EO at \mathcal{T} for the cases with and without a RIS. The CDF is evaluated as

$$F_{\text{EO}}(P_b) = \Pr((1 - \beta)P_T^* \leq P_b'). \quad (20)$$

When there is no RIS to power up the tag, the range is just ~ 6 m, and beyond 6 m, the tag goes to an EO. However, a RIS can lower the EO and achieve higher ranges than without a RIS case. For example, a RIS with 100 and 400 reflecting elements extends the tag activation range to 13 m and 34 m metres, respectively. Therefore, a RIS can prevent the risk of EO at the tag.

D. Average Achievable Rate

The achievable rate describes the bit rate a network can reliably transmit under a long-term, stable fading regime. This measure provides valuable insights into the use of specific

coding schemes. In the context of BiBC, it may help to identify feasible applications. The average achievable rate is the mean Shannon capacity given by

$$\mathcal{R} = \mathbb{E}\{\log_2(1 + \gamma^*)\}. \quad (21)$$

The exact derivation of the average achievable rate given in (21) seems intractable. However, by invoking Jensen's inequality, the tight upper and lower bounds are given as [50]

$$\mathcal{R}_{\text{lb}} \leq \mathcal{R} \leq \mathcal{R}_{\text{ub}}, \quad (22)$$

where \mathcal{R}_{lb} and \mathcal{R}_{ub} are respectively defined as

$$\mathcal{R}_{\text{lb}} = \log_2\left(1 + [\mathbb{E}\{1/\gamma^*\}]^{-1}\right), \quad (23a)$$

$$\mathcal{R}_{\text{ub}} = \log_2(1 + \mathbb{E}\{\gamma^*\}). \quad (23b)$$

where $\mathbb{E}\{\gamma^*\} = \bar{\gamma}\mu_\Lambda^{(2)}$, and

$$\mathbb{E}\{1/\gamma^*\} = \frac{1}{\mathbb{E}\{\gamma^*\}} + \frac{\sigma_{\gamma^*}^2}{[\mathbb{E}\{\gamma^*\}]^3}, \quad (24)$$

in which $\sigma_{\gamma^*}^2 = \bar{\gamma}^2\sigma_{\Lambda^2}^2$. To calculate $\sigma_{\gamma^*}^2$, we need to calculate $\sigma_{\Lambda^2}^2 = \mu_\Lambda^{(4)} - [\mu_\Lambda^{(2)}]^2$ of Λ . Specifically, when Λ is approximated with Gamma distribution, $\Lambda \sim \Gamma(k_\Lambda, \lambda_\Lambda)$, [49]

$$\mu_\Lambda^{(m)} = k_\Lambda^m \frac{\Gamma(m + k_\Lambda)}{\Gamma(k_\Lambda)}. \quad (25)$$

Remark 4. To gain further insights, we let the number of RIS elements grow without a bound. We observe that the transmit power can be scaled inversely proportional to the square of the number of IRS elements in this operating regime, i.e., $\lim_{N \rightarrow \infty} P = P_A/N^2$. This is the well-known squared power gain provided by the RIS [51]. Hence, the lower and upper rate bounds can be shown to approach an asymptotic limit using this transmit power scaling law as (Appendix B)

$$\lim_{N \rightarrow \infty} \mathcal{R}_{\text{lb}} = \mathcal{R}_\infty, \quad \text{and} \quad \lim_{N \rightarrow \infty} \mathcal{R}_{\text{ub}} = \mathcal{R}_\infty, \quad (26)$$

where \mathcal{R}_∞ is given in (27) with $\bar{\gamma}_A = \beta P_A/\sigma_z^2$ and $\eta = \eta_n, \forall n$.

E. Outage Probability

The EO at \mathcal{T} and rate/SNR outage at \mathcal{R} both affect the ability to deliver information reliably. An EO occurs when the received signal power falls below \mathcal{T} 's activation threshold (P_b). In contrast, the SNR outage probability is the probability that the instantaneous SNR falls below a threshold (γ_{th}). Mathematically, the outage is expressed as

$$P_{\text{out}} = P_{\text{out}}^{\text{EO}} + (1 - P_{\text{out}}^{\text{EO}}) P_{\text{out}}^{\text{SNR}}, \quad (28)$$

where $P_{\text{out}}^{\text{EO}} = \Pr\{(1 - \beta)P_T^* \leq P_b\}$ and $P_{\text{out}}^{\text{SNR}} = \Pr\{\gamma \leq \gamma_{\text{th}}\}$. A tight approximation to the outage (28) is obtained as

$$P_{\text{out}} \approx F_{P_T^*}(\gamma_{\text{th}}) + (1 - F_{P_T^*}(\gamma_{\text{th}})) F_{\gamma^*}(\gamma_{\text{th}}), \quad (29)$$

where $F_{\gamma^*}(r)$ and $F_{P_T^*}(r)$ are given in (18a).

$$\mathcal{R}_\infty = \log_2 \left(1 + \bar{\gamma}_A (\sigma_{\alpha_u}^2 + \mu_{\alpha_u}^2) \left(\eta \frac{\Gamma(m_g + 1/2)\Gamma(m_h + 1/2)}{\Gamma(m_g)\Gamma(m_h)} \sqrt{\frac{\Omega_g \Omega_h}{m_g m_h}} \right)^2 \right) \quad (27)$$

F. Average Bit/Symbol Error Rate

The average BER is the ratio between the number of bits received in error and the number of bits transmitted. This measure is widely used to assess the reliability and quality of wireless links. In this section, we derive the BER of the system for BPSK modulation, a simple yet robust modulation scheme. The conditional error probability of BPSK is given as $P_{\text{BER}}(\gamma) = \lambda Q(\sqrt{\nu\gamma})$, with $\lambda = 1$ and $\nu = 2$ [52]. The average BER of the system with BPSK, using Gamma distribution (17a), is thus given as (Appendix C)

$$\bar{P}_{\text{BER}}^{\text{Gamma}} = A_1 (2\bar{A})^{-\frac{k_\Lambda}{2}} \Gamma(k_\Lambda) \exp\left(\frac{\hat{B}_1^2}{8\bar{A}}\right) D_{-k_\Lambda}\left(\frac{\hat{B}_1^2}{\sqrt{2\bar{A}}}\right),$$

where $\bar{A} = A\nu\bar{\gamma}$, $\bar{B} = B\sqrt{\nu\bar{\gamma}}$, $A_1 = \exp(-C)/(\Gamma(k_\Lambda)\lambda_\Lambda^k)$, $\hat{B}_1 = \bar{B} + 1/\lambda_\Lambda$, in which $A = 0.3842$, $B = 0.7640$, and $C = 0.6964$. Note that the BER analysis above can be extended for higher-order modulation schemes such as QPSK and M -QAM [53], [54]. For brevity, such analyses are omitted here.

G. Achievable Diversity Order

The diversity order reveals how the BER or SNR outage probability decays with the SNR. It is defined as the negative slope of those measures in the high SNR regime as follows:

$$G_d = - \lim_{\bar{\gamma} \rightarrow \infty} \frac{\log(P_{\text{out}}^{\text{SNR}})}{\log(\bar{\gamma})} = - \lim_{\bar{\gamma} \rightarrow \infty} \frac{\log(\bar{P}_{\text{BER}})}{\log(\bar{\gamma})}. \quad (30)$$

We next derive the outage probability and BER in the high SNR domain. We use the first-order polynomial expansion of the PDF approximations.

Lemma 1. *The asymptotic Outage Probability and BER are respectively given as*

$$P_{\text{out}}^\infty = \frac{1}{\Gamma(k_\Lambda + 1)\lambda_\Lambda^{k_\Lambda}} \left(\frac{\gamma_{\text{th}}}{\bar{\gamma}} \right)^{k_\Lambda/2} + \mathcal{O}\left(\bar{\gamma}^{-(k_\Lambda/2+1)}\right), \quad (31)$$

and

$$\bar{P}_{\text{BER}}^\infty = (\lambda_E \bar{\gamma})^{-k_\Lambda/2} + \mathcal{O}\left(\bar{\gamma}^{-(k_\Lambda/2+1)}\right), \quad (32)$$

where $\lambda_E = \nu \left[(2^{k_\Lambda/2}/3 + (3/2)^{k_\Lambda/2}) C_1 \right]^{2/k_\Lambda}$ and $C_1 = \lambda \Gamma(k_\Lambda/2)/(8\Gamma(k_\Lambda)\lambda_\Lambda^{k_\Lambda})$.

Proof. See Appendix D. ■

Using (31), the diversity order G_d and the coding gain, O_c , are respectively given as $G_d = k_\Lambda/2$, and $O_c = 1/(\Gamma(k_\Lambda + 1)\lambda_\Lambda^{k_\Lambda})$ [55]. Besides, from (32) the array gain becomes $G_a = \lambda_E$.

Remark 5. *According to Section III-C, $k_\Lambda = \mu_\Lambda^2/\sigma_\Lambda^2$ and $\lambda_\Lambda = \sigma_\Lambda^2/\mu_\Lambda$. Thus, the diversity order G_d can be given in (33), where we assume that $\eta_n = \eta, n \in \mathcal{N}$. In (33), we define $\mu_{\alpha_a} \triangleq \Upsilon_a \zeta_a^{1/2}$, and $\sigma_{\alpha_a}^2 \triangleq \Upsilon_a \zeta_a$, where $\Upsilon_a =$*

$\Gamma(m_a + 1/2)/\Gamma(m_a)$ and $\bar{\Upsilon}_a = m_a - \Upsilon_a^2$ (16a). Besides, for $\eta_n = \eta, n \in \mathcal{N}$, $\mu_X = N\hat{\Upsilon}\zeta_g^{1/2}\zeta_h^{1/2}$, $\sigma_X^2 = N\Upsilon'\zeta_g\zeta_h$, where $\Upsilon \triangleq \eta\Upsilon_g\Upsilon_h$ and $\Upsilon' \triangleq \eta^2\Upsilon_h\Upsilon_g$.

To gain further insight, we let the number of RIS elements increase to a large limit, i.e., $N \rightarrow \infty$. After several mathematical manipulations, we have²

$$\lim_{N \rightarrow \infty} G_d = \frac{1}{2} \frac{\Upsilon_u^2}{\bar{\Upsilon}_u} = \frac{1}{2} \left(m_u \left(\frac{\Gamma(m_u)}{\Gamma(m_u + \frac{1}{2})} \right)^2 - 1 \right)^{-1}. \quad (34)$$

From (34), unexpectedly, we observe that the diversity order of the proposed RIS-assisted system (Fig. 2) is constant in the high regime of N and solely depends on the \mathcal{T} - \mathcal{R} channel parameters. This behavior is because \mathcal{T} acts as a keyhole/pinhole [4]. Hence, regardless of the number of RIS elements or antennas of \mathcal{E} , the rank of combined channels \mathcal{E} - \mathcal{T} and \mathcal{E} -RIS- \mathcal{T} becomes one. Therefore, this combined channel does not contribute to the diversity order because of keyhole channel properties [56].

The coding gain and array gain are similarly derived as

$$\lim_{N \rightarrow \infty} O_c = \frac{1}{\Gamma\left(\frac{\Upsilon_u^2}{\bar{\Upsilon}_u} + 1\right)} \left(N\hat{\Upsilon}\sqrt{\zeta_u\zeta_g\zeta_h}\bar{\Upsilon}_u\Upsilon_u^{-1} \right)^{-\frac{\Upsilon_u^2}{\bar{\Upsilon}_u}} \quad (35)$$

$$\lim_{N \rightarrow \infty} G_a = \lambda_{\bar{E}} \left(N\hat{\Upsilon}\sqrt{\zeta_u\zeta_g\zeta_h}\bar{\Upsilon}_u\Upsilon_u^{-1} \right)^{-2}, \quad (36)$$

where $\lambda_{\bar{E}} = \nu \left[\left(2\Upsilon_u^2/(2\bar{\Upsilon}_u)/3 + (3/2)\Upsilon_u^2/(2\bar{\Upsilon}_u) \right) C_{\bar{1}} \right]^{\frac{2\Upsilon_u^2}{\bar{\Upsilon}_u}}$, and $C_{\bar{1}} = \lambda \Gamma(\Upsilon_u^2/(2\bar{\Upsilon}_u))/(8\Gamma(\Upsilon_u^2/\bar{\Upsilon}_u))$.

From (35) and (36), while the diversity order is independent of the number of RIS elements, the coding gain and the array gain are both functions of it - see Fig. 8 and Fig. 9.

H. Effect of RIS Phase Quantization Errors

Due to hardware limitations and imperfect CSI, adopting continuous RIS phase shifts over $[-\pi, \pi]$ might be infeasible. Thus, phase shifts would be quantized to a set of discrete values [20], i.e., each RIS element uses only a finite number of phase shifts. Accordingly, the discrete phase of n -th RIS element is given as $\hat{\theta}^* = \kappa\pi/2^D$, where D represents the number of quantization bits, $\kappa = \min_{\theta \in \{0, \pm 1, \dots, \pm 2^{D-1}\}} |\theta^* - \theta\pi/2^D|$, and θ^* is the optimal phase shift, given in (10). Thus, the quantization error is $\epsilon_n = \theta_n^* - \hat{\theta}_n^*$, $n \in \mathcal{N}$, which can be shown to be uniformly distributed for large quantization levels, i.e., $\epsilon_n \sim \mathcal{U}[-\tau, \tau]$ and $\tau = \pi/2^D$ [57], [58]. Therefore, the optimal received SNR γ^* given in (12) with the discrete phase shifts may be expressed as

$$\begin{aligned} \gamma^* &= \bar{\gamma} \left| \alpha_u \left(\alpha_f + \sum_{n \in \mathcal{N}} \eta_n \alpha_{g_n} \alpha_{h_n} e^{j\epsilon_n} \right) \right|^2 \\ &= \bar{\gamma} \alpha_u^2 ((\alpha_f + X_R)^2 + X_I^2), \end{aligned} \quad (37)$$

²Note that G_d is derived using the Gamma approximation and letting N grow large. Hence, G_d may not be exact. However, since the exact derivation is mathematically intractable, this approximation provides valuable insights.

$$G_d = \frac{1}{2} \frac{\Upsilon_u^2 \zeta_u \left(\Upsilon_f \zeta_f^{1/2} + N \hat{\Upsilon} \zeta_g^{1/2} \zeta_h^{1/2} \right)^2}{\zeta_u \left(\tilde{\Upsilon}_u + \Upsilon_u^2 \right) \left(\tilde{\Upsilon}_f \zeta_f + N \Upsilon_f' \zeta_g \zeta_h \right) + \tilde{\Upsilon}_u \zeta_u \left(\Upsilon_f \zeta_f^{1/2} + N \hat{\Upsilon} \zeta_g^{1/2} \zeta_h^{1/2} \right)^2}, \quad (33)$$

where $X_R \triangleq \sum_{n \in \mathcal{N}} \eta_n \alpha_{g_n} \alpha_{h_n} \cos(\epsilon_n)$ and $X_I \triangleq \sum_{n \in \mathcal{N}} \eta_n \alpha_{g_n} \alpha_{h_n} \sin(\epsilon_n)$.

We investigate the effect of phase quantization errors at the RIS on the average achievable rate. According to Section III-D, we can derive an upper bound for the average achievable rate, given in (23a), with discrete phase shifts as follows:

$$\bar{\mathcal{R}}_{\text{ub}} = \log_2 \left(1 + \bar{\gamma} \mu_{\alpha_u}^{(2)} \left(\mu_{\alpha_f}^{(2)} + \mu_{X_R}^{(2)} + 2\mu_{\alpha_f} \mu_{X_R} + \mu_{X_I}^{(2)} \right) \right), \quad (38)$$

where $\mu_{X_R}^{(2)} = \sigma_{X_R}^2 + \mu_{X_R}^2$, $\mu_{X_I}^{(2)} = \sigma_{X_I}^2 + \mu_{X_I}^2$, and

$$\mu_{X_R} = \sum_{n \in \mathcal{N}} \eta_n \mu_{\alpha_{g_n}} \mu_{\alpha_{h_n}} \frac{\sin(\tau)}{\tau}, \quad (39a)$$

$$\sigma_{X_R}^2 = \sum_{n \in \mathcal{N}} \eta_n^2 \mu_{\alpha_{g_n}}^{(2)} \mu_{\alpha_{h_n}}^{(2)} \left(\frac{1}{2} + \frac{\sin(2\tau)}{4\tau} \right) - \mu_{X_R}^2, \quad (39b)$$

$$\sigma_{X_I}^2 = \sum_{n \in \mathcal{N}} \eta_n^2 \mu_{\alpha_{g_n}}^{(2)} \mu_{\alpha_{h_n}}^{(2)} \left(\frac{1}{2} - \frac{\sin(2\tau)}{4\tau} \right), \quad (39c)$$

where $\mu_{X_I} = 0$, and $\mu_{\alpha_a}^{(m)}$, $a \in \mathcal{A}$ is given in (16a).

Remark 6. If a RIS is placed in the \mathcal{T} - \mathcal{R} link of a BiBC setup, we can investigate the network's performance following a similar approach for the setup with RIS in the \mathcal{E} - \mathcal{T} link. However, when both the \mathcal{E} - \mathcal{T} and \mathcal{T} - \mathcal{R} links use RIS, the Gaussian and Gamma approximations may not match well with the exact PDF and CDF of the received SNR. We can still derive the upper and lower bounds of the average achievable rate using a similar method given in Section III-D.

IV. MULTI-TAG SYSTEM

This section develops the analysis of multiple ($K > 1$) single-antenna tags in Fig. 2. Here, by optimizing the RIS phase shifts, we simultaneously maximize the received signal power at \mathcal{T}_k and the achievable sum rate at \mathcal{R} . To this end, the problem is formulated as follows:

$$\mathcal{P}_{M,1} : \underset{\boldsymbol{\theta}}{\text{maximize}} \sum_{k \in \mathcal{K}} \log_2(1 + \gamma_k), \quad (40a)$$

$$\text{subject to } (1 - \beta)P_{T,k} \geq P'_b, \quad (40b)$$

$$|\bar{\theta}_n| \leq 1, \quad (40c)$$

where $P_{T,k}$ is given in (5), and γ_k is the signal-to-interference-plus-noise ratio (SINR) of \mathcal{T}_k at \mathcal{R} . Using (6), γ_k is obtained as

$$\gamma_k = \frac{\beta P |u_k (f_k + \mathbf{g}_k^T \boldsymbol{\theta})|^2}{\sum_{i \in \mathcal{K}/k} \beta P |u_i (f_i + \mathbf{g}_i^T \boldsymbol{\theta})|^2 + \sigma_z^2}. \quad (41)$$

In (40), the constraint (40b) guarantees the minimum power for \mathcal{T}_k .

Because of the non-convex objective function and the constraint, $\mathcal{P}_{M,1}$ is not amenable to popular convex algorithms. Therefore, we develop a solution based on fractional programming.

A. Proposed Solution

First, we define $\mathbf{a}_k \triangleq \text{diag}(u_k \mathbf{g}_k^T) \mathbf{h}$ and $b_k \triangleq u_k f_k$. Thereby, the SINR (41) is rearranged as

$$\gamma_k = \frac{\beta P |b_k + \boldsymbol{\theta}^H \mathbf{a}_k|^2}{\sum_{i \in \mathcal{K}/k} \beta P |b_i + \boldsymbol{\theta}^H \mathbf{a}_i|^2 + \sigma_z^2}, \quad (42)$$

where $\boldsymbol{\theta} = [\bar{\theta}_1, \dots, \bar{\theta}_N]^T$. Then, $\mathcal{P}_{M,1}$ can be treated as a fractional programming problem [30], [59]. We next apply a quadratic transform to the objective function of $\mathcal{P}_{M,1}$ as

$$f(\boldsymbol{\theta}, \boldsymbol{\lambda}) = \sum_{k \in \mathcal{K}} \log_2 \left(1 + 2\lambda_k \sqrt{\beta P} \text{Re} \{ b_k + \boldsymbol{\theta}^H \mathbf{a}_k \} - \lambda_k^2 \left(\beta P \sum_{i \in \mathcal{K}/k} |b_i + \boldsymbol{\theta}^H \mathbf{a}_i|^2 + \sigma_z^2 \right) \right), \quad (43)$$

where $\boldsymbol{\lambda} = [\lambda_1, \dots, \lambda_K]^T$ is auxiliary variables introduced by the quadratic transformation. Thereby, we alternatively optimize $\boldsymbol{\theta}$ and $\boldsymbol{\lambda}$. For a given $\boldsymbol{\theta}$, the optimal λ_k is found in closed-form as [30], [59]

$$\lambda_k^* = \frac{\sqrt{\beta P} \text{Re} \{ b_k + \boldsymbol{\theta}^H \mathbf{a}_k \}}{\ln(2) \left(\beta P \sum_{i \in \mathcal{K}/k} |b_i + \boldsymbol{\theta}^H \mathbf{a}_i|^2 + \sigma_z^2 \right)}. \quad (44)$$

Remark 7. Without losing generality, we constrain the phase-shift vector, $\boldsymbol{\theta}$, with the channel responses to obtain a non-negative real desired signal term, i.e., $|b_k + \boldsymbol{\theta}^H \mathbf{a}_k| \approx \text{Re} \{ b_k + \boldsymbol{\theta}^H \mathbf{a}_k \}$. Our simulation results also support the validity of this approach. This is due to the fact that our method iteratively maximizes the achievable rate/SINR by co-phasing the desired signal component while reducing interference.

Next, we must optimize $\boldsymbol{\theta}$ for a given $\boldsymbol{\lambda}$. First, by expanding $|b_k + \boldsymbol{\theta}^H \mathbf{a}_k|^2$ and then applying several mathematical manipulations, the objective function in (43) can be rearranged as

$$f(\boldsymbol{\theta}) = \sum_{k \in \mathcal{K}} \log_2 \left(1 - \boldsymbol{\theta}^H \mathbf{U}_k \boldsymbol{\theta} + 2 \text{Re} \{ \boldsymbol{\theta}^H \mathbf{v}_k \} + c_k \right), \quad (45)$$

where \mathbf{U}_k , \mathbf{v}_k , and c_k are defined as

$$\mathbf{U}_k \triangleq 2(\lambda_k^*)^2 \beta P \sum_{i \in \mathcal{K}/k} \mathbf{a}_i \mathbf{a}_i^H, \quad (46a)$$

$$\mathbf{v}_k \triangleq \lambda_k^* \sqrt{\beta P} \mathbf{a}_k - (\lambda_k^*)^2 \beta P \sum_{i \in \mathcal{K}/k} b_i^* \mathbf{a}_i,$$

$$c_k \triangleq 2\lambda_k^* \sqrt{\beta P} \text{Re} \{ b_k \} - (\lambda_k^*)^2 \left(\beta P \sum_{i \in \mathcal{K}/k} |b_i|^2 + \sigma_z^2 \right). \quad (46b)$$

Next, the corresponding optimization problem is given as

$$\mathcal{P}_{M,2} : \underset{\boldsymbol{\theta}}{\text{maximize}} f(\boldsymbol{\theta}), \quad (47a)$$

$$\text{subject to } (1 - \beta)P_{T,k}^{\text{Lin}} \geq P'_b, \quad (47b)$$

$$|\bar{\theta}_n| \leq 1, \quad (47c)$$

TABLE II: Simulation settings.

Parameter	Value	Parameter	Value
f_c	3 GHz	$\eta_n, \forall n$	0.8
B	10 MHz	d_f, d_u	10, 5 m
N_f	10 dB	d_g, d_h	3, 8 m
$m_a, a \in \mathcal{A}$	3	β, ϕ	0.6, 0.8

where $P_{T,k}^{\text{Lin}}$ is the linearized received signal power at \mathcal{T}_k , given as

$$P_{T,k}^{\text{Lin}} = \boldsymbol{\theta}_{j-1}^H \bar{\mathbf{U}}_k \boldsymbol{\theta}_{j-1} + 2\text{Re} \{ \boldsymbol{\theta}_{j-1}^H \bar{\mathbf{v}}_k \} + \bar{c}_k + ((\bar{\mathbf{U}}_k + \bar{\mathbf{U}}_k^H) \boldsymbol{\theta}_{j-1} + 2\text{Re} \{ \bar{\mathbf{v}}_k \})^H (\boldsymbol{\theta}_j - \boldsymbol{\theta}_{j-1}), \quad (48)$$

where $\bar{\mathbf{a}}_k \triangleq \text{diag}(\mathbf{g}_k^T) \mathbf{h}$, $\bar{b}_k \triangleq f_k$, $\bar{\mathbf{U}}_k \triangleq P \bar{\mathbf{a}}_k \bar{\mathbf{a}}_k^H$, $\bar{\mathbf{v}}_k \triangleq P \bar{b}_k^* \bar{\mathbf{a}}_k$, and $\bar{c}_k \triangleq P |b_k|^2$. Besides, $\boldsymbol{\theta}_j$ and $\boldsymbol{\theta}_{j-1}$ are the current and the previous iteration values of $\boldsymbol{\theta}$.

Because $\mathbf{a}_k \mathbf{a}_k^H$ is a positive-definite matrix, \mathbf{U}_k is also a positive-definite matrix. Hence, the objective function, $f(\boldsymbol{\theta})$, is a quadratic concave function of $\boldsymbol{\theta}$. Thus, \mathcal{P}_2 can be solved as a quadratically constrained quadratic program (QCQP) [60], see Algorithm 1.

Algorithm 1 : Algorithm for phase shift optimization.

Initialization: Initialize $\boldsymbol{\theta}$ to a feasible value.

Repeat

Step 1: Update $\boldsymbol{\lambda}$ by (44).

Step 2: Update $\boldsymbol{\theta}$ by solving \mathcal{P}_2 in (47).

Until the value of the objective function converges.

Output: The optimal phase shift matrix Θ° .

Remark 8. The proposed optimization approach for solving Θ is presented in Algorithm 1 after the original problem, $\mathcal{P}_{M,1}$, is transformed into a convex problem. $\mathcal{P}_{M,1}$ is solved iteratively using an alternate optimization technique. First, we calculate the SINR in (42) after we initiate Θ to a feasible value, and then we update a better solution for Θ in each iteration. This process is repeated until the normalized objective function increases by less than $\epsilon = 10^{-4}$.

Remark 9. Because the tags are passive devices with limited power, $\mathcal{P}_{M,1}$ considers fixed reflection coefficients, β_k 's, to keep the tags' power, cost, and form factor to a minimum [61]. β_k 's, however, can be optimized at the expense of a simple tag architecture. We can easily utilize alternative optimization because Θ and β_k 's are independent variables. Thereby, Θ and β_k 's are alternately optimized till convergence. For the sake of brevity, we omit details.

B. Computational Complexity

The proposed algorithm is an alternating optimization solution with iterative multiple stages. The outer loop optimizes Θ . This sub-problem requires iterative updates. The computational complexity of Algorithm 1 is centered in step 2. As CVX (MATLAB) uses the SDPT3 solver for this, the computational complexity of Algorithm 1 is $\mathcal{O}(N^3)$ [62]. Thus, the total complexity is $\mathcal{O}(I_\theta N^3)$, where I_θ is the number of iterations of Algorithm 1.

V. SIMULATION RESULTS

We adopt the 3GPP UMi model to model the large-scale fading ζ_a for $a \in \mathcal{A}$ with $f_c = 3$ GHz operating frequency

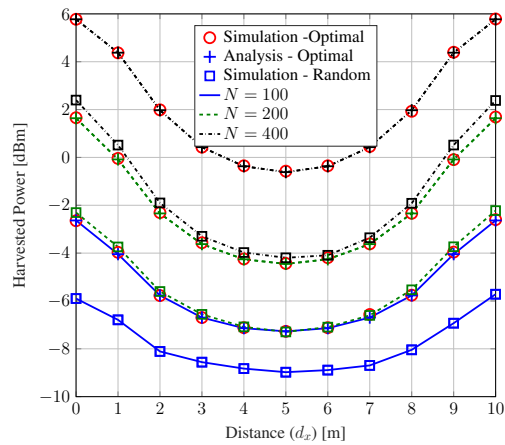


Fig. 5: The harvested power for $P = 20$ dBm, $d_f = 10$ m, $d_u = 5$ m, $d_h = \sqrt{d_y^2 + d_x^2}$, $d_g = \sqrt{d_y^2 + (d_f - d_x)^2}$, and $d_y = 1$ m.

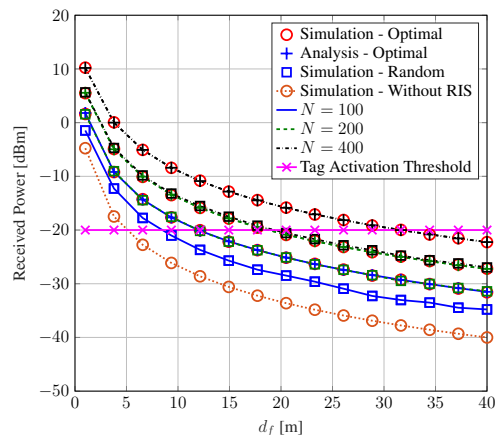


Fig. 6: The average received signal power at the tag as a function of \mathcal{E} - \mathcal{T} distance (d_f) for $P = 20$ dBm, $d_h = 1$ m, and $d_g = \sqrt{d_h^2 + (d_f)^2}$.

[63, Table B.1.2.1]. The AWGN variance, σ_z^2 , is modeled as $\sigma_z^2 = 10 \log_{10}(N_0 B N_f)$ dBm, where $N_0 = -174$ dBm/Hz, B is the bandwidth, and N_f is the noise figure. Unless otherwise specified, Table II gives the simulation parameters. To ensure statistical consistency, we generate the simulation curves by averaging over 10^5 iterations except for outage and BER, where we use 10^8 iterations. As a benchmark, we also consider random RIS phase-shifts, i.e., $\theta_n \in \mathcal{U}[-\pi, \pi]$.

A. Single-Tag Scenario

1) **RIS Location:** Fig. 5 explores the optimal RIS location using both optimal and random phase-shift designs. The harvested power at \mathcal{T} , which is computed using (14), is plotted as a function of the RIS placement in the power-up link. Monte-Carlo simulation is performed to validate the accuracy of the harvested power analysis. The results demonstrate that the optimal placement of the RIS should be near either \mathcal{E} or \mathcal{T} , while placing the RIS in the middle of the \mathcal{E} - \mathcal{T} link leads to the lowest harvested power and, consequently, the poorest rate performance. Optimal RIS phase-shifts result in a substantial improvement in harvested power compared to the random phase-shift design.

2) **Passive Tag Activation Range:** In Fig. 6, we present the received signal power at \mathcal{T} as a function of the \mathcal{E} - \mathcal{T} distance (d_f) for different RIS sizes. We include a comparison case without RIS. To provide valuable insights, we depict the activation threshold of \mathcal{T} (typically around -20 dBm for commercial passive RFID tags [6]). Without a RIS, the range of \mathcal{T} is limited to less than 6 m as the received power at the tag is insufficient for activation beyond this distance. However, the presence of an RIS between \mathcal{E} and \mathcal{T} significantly increases this range. For RIS sizes 100 and 400 and optimized phase shifts, \mathcal{T} 's activation distance increases 13 m and 34 m, respectively. However, with random phase shifts, it reduces to 9 m and 20 m respectively. These gains highlight the effectiveness of our proposed design.

3) **Performance Evaluation:** Fig. 7 depicts the average rate gain offered by the RIS against the non-RIS scenario as a function of the number of RIS elements N for different \mathcal{E} 's transmit power P . The achievable rate gain is calculated as $\mathcal{R}_{\text{ub}}^{\text{RIS}} - \mathcal{R}_{\text{ub}}^{\text{non-RIS}}$, where $\mathcal{R}_{\text{ub}}^{\text{RIS}}$ is the achievable rate upper bound with a RIS in the forward link and $\mathcal{R}_{\text{ub}}^{\text{non-RIS}}$ is the achievable rate upper bound of non-RIS setup. As observed, deploying a RIS in the forward link (\mathcal{E} - \mathcal{T} link) can considerably increase the achieved rate of \mathcal{T} . Moreover, with increasing N , \mathcal{T} can achieve a higher rate gain due to the increased received power at \mathcal{T} , which eventually increases the received SNR. This suggests that a large RIS is more beneficial. Specifically, at $P = 10$ dBm, a RIS with 200 and 300 elements provides respectively a gain of 1.5 bps/Hz and 2.1 bps/Hz.

Fig. 8 depicts the outage probability as a function of transmit power P for various numbers of RIS elements. It includes the analytical outage curves obtained using the closed-form expression (29), as well as the Monte-Carlo simulated curves and the Gaussian approximation for comparison. The outage probability of \mathcal{E} - \mathcal{T} - \mathcal{R} transmission in a non-RIS setup is provided as a reference. The figure demonstrates that the Gaussian and Gamma approximations closely align with the exact outage curves, particularly for low-to-moderate transmit power levels of the emitter. As expected, the proposed RIS-aided system significantly improves the outage performance compared to the non-RIS counterpart. Moreover, with optimal RIS phase-shifts, the outage performance is further enhanced, providing a minimum power gain of 5 dBm and 14 dBm when compared to the random phase shift design and the non-RIS case.

In Fig. 9, we present the average BER of BPSK as a function of the transmit power P for different numbers of RIS elements. The analytical BER curves, obtained using the closed-form expression (30), are plotted along with the analytical BER curves for the Gaussian approximation. Additionally, the exact BER curves are generated through Monte Carlo simulations. We include the BER performance of \mathcal{E} - \mathcal{T} - \mathcal{R} transmission in a non-RIS setup for comparison. The asymptotic behavior of the average BER in the high power (SNR) regime is also examined using (32). From Fig. 9, it can be observed that the analytical BER curves, under both approximations, closely match the exact BER curve for low-to-moderate transmit power of \mathcal{E} . For high transmit power of \mathcal{E} , the BER under

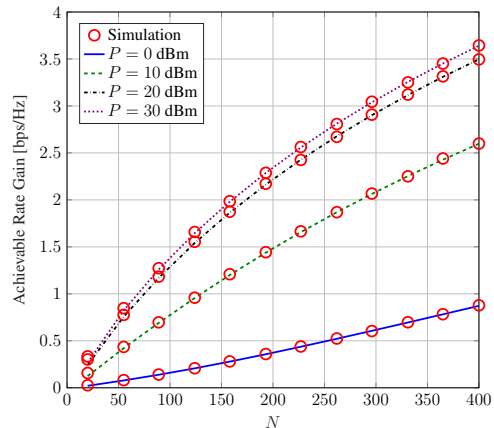


Fig. 7: The rate gain compared to the non-RIS case for $d_f = 10$ m, $d_u = 5$ m, $d_h = 8$ m, and $d_g = 3$ m.

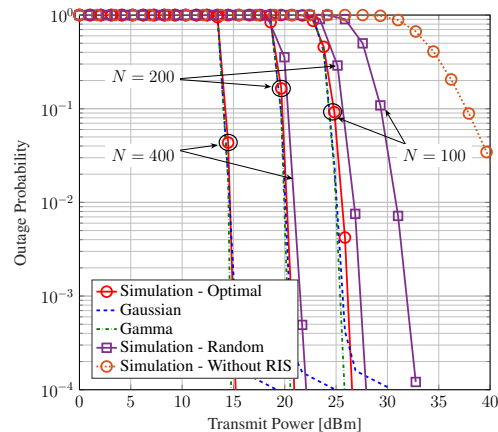


Fig. 8: The outage probability for $\gamma_{th} = 0$ dB, $d_f = 8$ m, $d_u = 4$ m, $d_h = 1$ m, and $d_g = 8$ m.

Gaussian and Gamma approximations serve as upper and lower bounds, respectively, for the exact average BER of the RIS-assisted system. The asymptotic BER probability curves provide insights into the achievable diversity orders.

Fig. 8 and Fig.9 demonstrate that the proposed system outperforms the non-RIS setup in terms of the outage and BER performance given the same transmit power, or the former achieves the same outage and BER performance as the latter with much less transmit power. For instance, achieving a 10^{-2} BER requires 19 dBm in the non-RIS setup, whereas the same can be achieved with a RIS ($N = 100$) at only 5 dBm. This amounts to a power saving of 14 dB. Furthermore, increasing the size of the RIS enhances the outage and BER performance. From a green perspective, using a RIS to energize the tags improves reliability, reduces the required transmit power for a specific BER, and extends the communication range.

4) **The effect phase discretization:** Fig. 10 examines the impact of RIS phase quantization error on the average achievable rate for different numbers of quantization bits (D) and RIS elements (N). The plot shows the percentage rate ratio against the average transmit power, which is defined as $\hat{\mathcal{R}} = \mathcal{R}_{\text{ub}} / \mathcal{R}_{\text{ub}} \times \%100$, where \mathcal{R}_{ub} is the average achievable

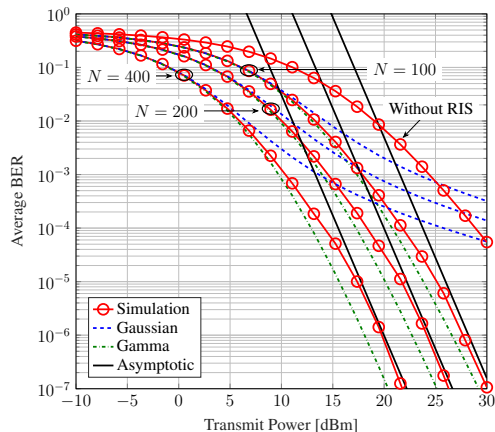


Fig. 9: BER of BPSK for $d_f = 10$ m, $d_u = 5$ m, $d_h = 8$ m, and $d_g = 3$ m.

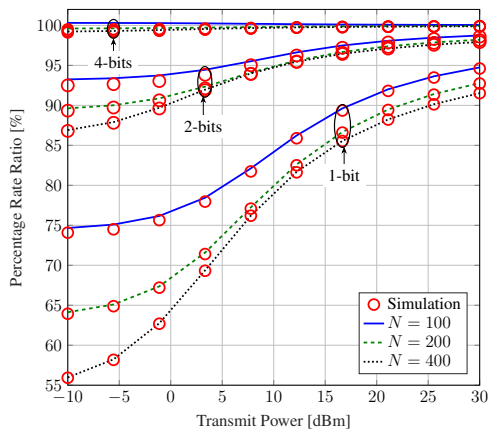


Fig. 10: The effect of phase quantization on the rate for $D = \{1, 2, 4\}$ bit, $d_f = 10$ m, $d_u = 5$ m, $d_h = 8$ m, and $d_g = 3$ m.

rate upper bound with phase shift quantization errors given in (38) and \mathcal{R}_{ub} denotes the upper bound of the achievable rate with continuous phase shifts in (22b). The results are validated through Monte-Carlo simulations. As the number of quantization bits (D) increases, the effect of quantization error becomes negligible. For $D = 4$, nearly 100% of the rate with continuous phase shifts can be achieved, rendering the quantization error negligible. Additionally, as expected, the impact of phase quantization error intensifies with increasing RIS size and for fixed quantization level.

B. Multi-Tag Scenario

Fig. 11 and Fig. 12 show the outage and BER performance of our proposed RIS-aided system with two tags ($K = 2$), which significantly improves their outage and rate performances compared to the non-RIS setup. Our optimal RIS phase-shift design for a RIS with 100 elements clearly outperforms the other options, e.g., resulting in a reduction in the outage of 37.2% and 55.1% compared to the random phase-shift case and the no-RIS case at a transmit power of $P = 30$ dBm, respectively. Furthermore, when the RIS elements increase to 200 and 400 with optimal phase-shift

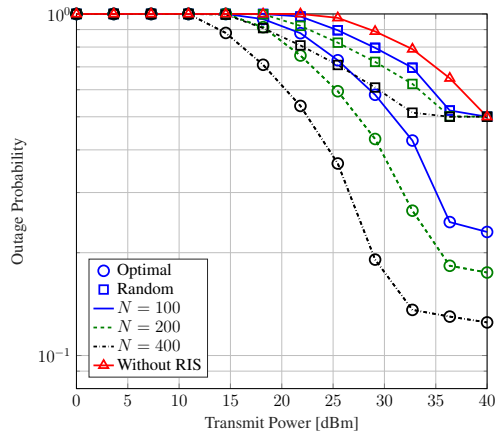


Fig. 11: The outage probability for $K = 2$, $\gamma_{th} = 0$ dB, $d_{f_k} = \{4, 5\}$ m, $d_{u_k} = \{5, 5\}$ m, $d_h = 2$ m, and $d_{g_k} = \{4.5, 5.4\}$ m.

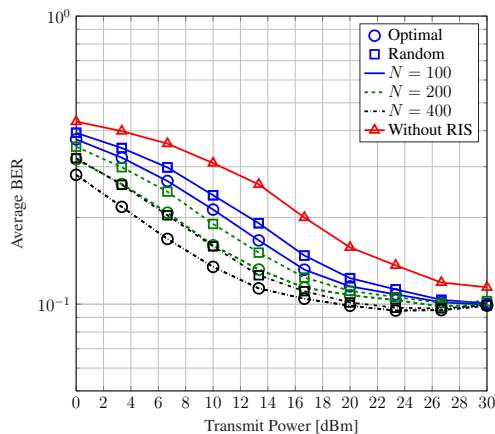


Fig. 12: BER of BPSK for $K = 2$, $d_{f_k} = \{4, 5\}$ m, $d_{u_k} = \{5, 5\}$ m, $d_h = 2$ m, and $d_{g_k} = \{4.5, 5.4\}$ m.

design, an additional outage reduction of 108.6% and 368.0% is achieved at the same transmit power. On the other hand, increasing the number of elements with the random phase-shift design does not yield significant improvement. Therefore, the proposed optimal phase-shift design, RIS placement in the emitter-to-tag path, and increasing the number of its elements prove to be an effective and green solution for passive IoT networks.

Figs. 11 and 12 also indicate that the reliability of the system in the high SNR regime is limited by interference between tags. Increasing the size of the RIS alone does not provide a solution. However, one effective approach is to employ a multi-antenna emitter and reader. This enables optimal energy beamforming and receive filtering in the spatial domain, allowing interference suppression and performance enhancement. This is a fertile future research direction.

VI. CONCLUSION

Passive tags face drawbacks such as activation failures, limited activation distances, and low data rates due to energy scarcity. To address these issues, we explored the use of a RIS

to enhance the RF signal power received by the tags. We employed a linear EH model and developed analytical techniques to quantify the benefits of RIS deployment. Specifically, we statistically analyzed the maximum received power at the tag and optimized the SNR at the reader. We derived performance metrics such as achievable rate, outage probability, BER, and diversity order for the system. Additionally, we examined the impact of RIS phase shift errors and proposed a RIS optimization algorithm for multi-tag networks. Overall, the use of a RIS can significantly enhance the received power at the tag, thereby increasing activation distances, achievable rates, and communication ranges. Importantly, these improvements can be achieved while maintaining the fundamental design of the tags, which preserves their cost, size, form factor, and batteryless advantages. Some of the specific insights into the use of the RIS are as follows.

- 1) The low activation distance (that is, less than 6 m) can be improved (Fig. 6). For example, 100 and 400 elements improve it to 13 m and 34 m for a single tag. RIS also improves rate, outage, and BER. Compared to the non-RIS setup, for $P = 20$ dBm, 200 RIS elements and a BPSK tag can achieve a rate gain of 2.2 bps/Hz (Fig. 7), an outage probability gain of $\sim 10^2$ (Fig. 8), and a BER gain of $\sim 10^{4.6}$ (Fig. 9).
- 2) The diversity order is independent of the number of RIS elements, N . However, the coding and array gains depend on N (Fig. 9). The optimal placement of the RIS is found to be as close to the emitter or the tags as possible (Fig. 5).
- 3) When imperfect channel estimates and hardware limitations are present, continuous phase shifts over the entire interval of $[0, 2\pi]$ are not feasible. Discrete phase shifts with various quantization levels can then be employed. Fortunately, even $D = 4$ has negligible performance degradation (Figure 10).

These insights address the rate requirement, reliability, and coverage, for establishing passive IoT. Our study spurs further research into the following topics:

- 1) *Imperfect CSI and Interference Cancellation*: The assumption of perfect CSI yields the upper bounds of the performance metrics. However, especially for multiple tags, accurate CSI acquisition is challenging. introduces residual interference in the direct \mathcal{E} - \mathcal{R} link and the reflected RIS- \mathcal{R} link. With our analytical tools, interference cancellation techniques could be developed (Section II-A). The imperfect CSI case should be researched.
- 2) *Active RIS*: Using an active RIS or a hybrid RIS which combines both active and passive elements, can further improve the tag activation and system performance. However, the total energy consumption must be considered especially for green networks. This is a potential future extension of this work.
- 3) *Multiple-Antenna Nodes*: We considered only signal-antenna tags and the emitter (Fig. 2). However, the use of multiple antennas offers spatial diversity gains that can be exploited to enhance performance. Thus, energy beamforming and reception filters can be designed at the

emitter and reader to not only deliver more power to the passive tags but also suppress the mutual interference between tags and enhance performance.

APPENDIX

A. Gaussian Approximation

First, we find the mean and the variance of Λ . Since Λ is a product of two independent variables, we find that $\mu_\Lambda = \mu_{\alpha_u} \mu_Y$, and $\sigma_\Lambda^2 = \mu_{\alpha_u}^2 \mu_Y^2 - \mu_Y^2 \mu_{\alpha_u}^2$, where $\mu_Y = \mu_{\alpha_f} + \mu_X$, $\mu_{\alpha_u}^{(2)} = \sigma_{\alpha_u}^2 + \mu_{\alpha_u}^2 (16a)^3$, $\mu_Y^{(2)} = \sigma_Y^2 + \mu_Y^2$, and $\sigma_Y^2 = \sigma_{\alpha_f}^2 + \sigma_X^2$.

Direct Gaussian approximations do not work here. Thus, our approach involves two steps: (i) we use the moment matching technique to approximate Y and Λ as Gaussian variables with $Y \sim \mathcal{N}(\mu_Y, \sigma_Y^2)$ and $\Lambda \sim \mathcal{N}(\mu_\Lambda, \sigma_\Lambda^2)$. (ii) however, since Y and Λ are positive random variables, i.e., $Y, \Lambda \geq 0$, we truncate the approximated Gaussian distribution such that it only lies within the interval $[0, \infty)$, i.e., positive real axis [48], [49]. Hence the approximated CDF and PDF of Y and Λ are respectively given as

$$F_C(r) = 1 - \Psi Q\left(\frac{r - \mu_C}{\sigma_C}\right), \quad (49a)$$

$$f_C(r) = \frac{\Psi}{\sqrt{2\pi}\sigma_C} \exp\left(-\frac{(r - \mu_C)^2}{2\sigma_C^2}\right), \quad (49b)$$

for $r \geq 0$ and $C \in \{Y, \Lambda\}$. Here, $\Psi = 1/Q(-\mu_C/\sigma_C)$ achieves normalization: $\int_0^\infty f_C(x) dx = 1$.

B. Asymptotic Achievable Rate

When the RIS size increases indefinitely, i.e., $N \rightarrow \infty$, μ_X and σ_X^2 can be approximated as

$$\mu_X \approx N \left(\eta \frac{\Gamma(m_g + 1/2)\Gamma(m_h + 1/2)}{\Gamma(m_g)\Gamma(m_h)} \sqrt{\frac{\Omega_g \Omega_h}{m_g m_h}} \right) = N \bar{\mu}_X \quad (50)$$

$$\sigma_X^2 \approx N \left(\eta^2 \frac{\Gamma(m_g + 1)\Gamma(m_h + 1)}{\Gamma(m_g)\Gamma(m_h)} \frac{\Omega_g \Omega_h}{m_g m_h} - \bar{\mu}_X^2 \right) = N \bar{\sigma}_X^2 \quad (51)$$

where $\eta = \eta_n, \forall n$. Next, the SNR in \mathcal{R}_{ub} can be asymptotically evaluated as

$$\begin{aligned} \lim_{N \rightarrow \infty} \gamma_{ub} &= \lim_{N \rightarrow \infty} N^2 \bar{\gamma} (\sigma_{\alpha_u}^2 + \mu_{\alpha_u}^2) \\ &\quad \times \left(\frac{\sigma_{\alpha_f}^2}{N^2} + \frac{\bar{\sigma}_X^2}{N} + \frac{\mu_{\alpha_f}^2}{N^2} + \frac{2\mu_{\alpha_f} \bar{\mu}_X}{N} + \bar{\mu}_X^2 \right) \\ &= \bar{\gamma}_A (\sigma_{\alpha_u}^2 + \mu_{\alpha_u}^2) \bar{\mu}_X^2, \end{aligned} \quad (52)$$

where $\bar{\gamma}_A = \beta P_A / \sigma_z^2$ and $\lim_{N \rightarrow \infty} P = P_A / N^2$. Similarly, we can show that the SNR of the rate lower bound converges for the same asymptotic SNR, i.e., $\lim_{N \rightarrow \infty} \gamma_{lb} = \bar{\gamma}_A (\sigma_{\alpha_u}^2 + \mu_{\alpha_u}^2) \bar{\mu}_X^2$. Then, the asymptotic achievable rate can be derived as given in (27).

³For Nakagami- m_a α_a given in (2), $\alpha_a^2 \sim \Gamma(k, \lambda)$, where $k = m_a$ and $\lambda = \Omega_a / m_a$, with $\mu_{\alpha_a^2} = k\lambda$ and $\sigma_{\alpha_a^2}^2 = k\lambda^2$.

C. Average BER

The average BER of the system with BPSK is given as

$$\begin{aligned} \bar{P}_{\text{BER}} &= \mathbb{E}\{\lambda Q(\sqrt{\nu\gamma})\} \stackrel{(a)}{=} \int_0^\infty \lambda Q(x\sqrt{\nu\gamma}) f_\Lambda(x) dx \\ &\stackrel{(b)}{=} \int_0^\infty \lambda \exp(-A\nu\bar{\gamma}x^2 - B\sqrt{\nu\bar{\gamma}}x - C) f_\Lambda(x) dx, \end{aligned} \quad (53)$$

where (a) is due to submitting $\gamma = \bar{\gamma}\Lambda^2$ and $f_\Lambda(r)$ is given in (17a). Besides, Q function is substituted with its tight approximation: $Q(x) = \exp(-Ax^2 - Bx - C)$, where $A = 0.3842$, $B = 0.7640$ and $C = 0.6964$ [64].

By using the PDF of Λ given in (17a), we have

$$\begin{aligned} \bar{P}_{\text{BER}}^{\text{Gamma}} &= A_1 \int_0^\infty \exp(-\bar{A}x^2 - \bar{B}x) x^{k_\Lambda - 1} \exp\left(-\frac{x}{\lambda_\Lambda}\right) dx \\ &= A_1 \int_0^\infty \exp(-\bar{A}x^2 - \hat{B}_1 x) x^{k_\Lambda - 1} dx \\ &\stackrel{(d)}{=} A_1 (2\bar{A})^{-\frac{k_\Lambda}{2}} \Gamma(k_\Lambda) \exp\left(\frac{\hat{B}_1^2}{8\bar{A}}\right) D_{-k_\Lambda} \left(\frac{\hat{B}_1}{\sqrt{2\bar{A}}}\right) \end{aligned} \quad (54)$$

where $\bar{A} = A\nu\bar{\gamma}$, $\bar{B} = B\sqrt{\nu\bar{\gamma}}$, $A_1 = \exp(-C)/(\Gamma(k_\Lambda)\lambda_\Lambda^k)$, and $\hat{B}_1 = \bar{B} + 1/\lambda_\Lambda$. Beside, (d) is obtained by using the integral [31, eq. (3.462.1)].

D. Asymptotic Outage probability and BER

In order to derive the outage probability and BER in the high SNR domain, we use the first-order polynomial expansion of the PDF approximations.

Asymptotic SNR Outage Probability: this can be approximated as [55]

$$\lim_{\bar{\gamma} \rightarrow \infty} P_{\text{out}}^{\text{SNR}} = P_{\text{out}}^\infty \approx O_c \left(\frac{\gamma_{\text{th}}}{\bar{\gamma}}\right)^{G_d} + \mathcal{O}\left(\bar{\gamma}^{-(G_d+1)}\right), \quad (55)$$

where G_d is the diversity order and O_c is a measure of the coding gain [55]. By approximating the PDF of Λ for $r \rightarrow 0^+$ as $f_\Lambda^{0^+}(r) = 1/\Gamma(k_\Lambda)\lambda_\Lambda^{k_\Lambda} r^{k_\Lambda-1} + \mathcal{O}(r^{k_\Lambda})$, P_{out}^∞ is derived as

$$P_{\text{out}}^\infty = \frac{1}{\Gamma(k_\Lambda + 1)\lambda_\Lambda^{k_\Lambda}} \left(\frac{\gamma_{\text{th}}}{\bar{\gamma}}\right)^{k_\Lambda/2} + \mathcal{O}\left(\bar{\gamma}^{-(k_\Lambda/2+1)}\right), \quad (56)$$

where the diversity order, $G_d = k_\Lambda/2$, and the coding gain, $O_c = 1/(\Gamma(k_\Lambda + 1)\lambda_\Lambda^{k_\Lambda})$.

Asymptotic Average BER: The BER can be asymptotically approximated as [55]

$$\lim_{\bar{\gamma} \rightarrow \infty} P_{\text{BER}} = \bar{P}_{\text{BER}}^\infty \approx (G_a \bar{\gamma})^{-G_d} + \mathcal{O}\left(\bar{\gamma}^{-(G_d+1)}\right), \quad (57)$$

where G_a is the array gain. Thereby, the asymptotic BER is derived as

$$\begin{aligned} \bar{P}_{\text{BER}}^\infty &= \int_0^\infty \lambda Q(x\sqrt{\nu\bar{\gamma}}) f_\Lambda^{0^+}(x) dx \\ &\stackrel{(e)}{=} (\lambda_E \bar{\gamma})^{-k_\Lambda/2} + \mathcal{O}\left(\bar{\gamma}^{-(k_\Lambda/2+1)}\right), \end{aligned} \quad (58)$$

where $\lambda_E = \nu \left[(2^{k_\Lambda/2}/3 + (3/2)^{k_\Lambda/2}) C_1 \right]^{2/k_\Lambda}$ and $C_1 = \lambda \Gamma(k_\Lambda/2) / (8\Gamma(k_\Lambda)\lambda_\Lambda^{k_\Lambda})$. Moreover, (e) is obtained by substituting Q function with its tight approximation: $Q(x) = \exp(-x^2/2)/12 + \exp(-2x^2/3)/4$ [64]. Then, the array gain, $G_a = \lambda_E$.

REFERENCES

- [1] D.-L. Yang, F. Liu, and Y.-D. Liang, "A survey of the internet of things," in *Proc. of the 1st Int. Conf. on E-Business Intelli. (ICEBI 2010)*. Atlantis Press, Dec. 2010/12, pp. 524–532. [Online]. Available: <https://doi.org/10.2991/icebi.2010.72>
- [2] A. Al-Fuqaha, M. Guizani, M. Mohammadi, M. Aledhari, and M. Ayyash, "Internet of things: A survey on enabling technologies, protocols, and applications," *IEEE Commun. Surveys Tuts.*, vol. 17, no. 4, pp. 2347–2376, 4th Quart. 2015.
- [3] "3GPP TSG RAN Meeting –94e, Study proposal on passive IoT, 8A.1 (from RP-213368)," Dec. 2021. Available Online: <https://www.3gpp.org/DynaReport/TDocExMtg--RP-94-e--60214.htm>.
- [4] D. Galappaththige, F. Rezaei, C. Tellambura, and S. Herath, "Link budget analysis for backscatter-based passive IoT," *IEEE Access*, vol. 10, pp. 128 890–128 922, Dec. 2022.
- [5] F. Rezaei, D. Galappaththige, C. Tellambura, and S. Herath, "Coding techniques for backscatter communications - A contemporary survey," *IEEE Commun. Surveys Tuts.*, pp. 1020–1058, 2th Quart. 2023.
- [6] "GAO RFID Inc." Available Online: <https://gaorfid.com/>.
- [7] S. Wang, M. Xia, K. Huang, and Y.-C. Wu, "Wirelessly powered two-way communication with nonlinear energy harvesting model: Rate regions under fixed and mobile relay," *IEEE Trans. Wireless Commun.*, vol. 16, pp. 8190–8204, Dec. 2017.
- [8] J. Kimionis, A. Bletsas, and J. N. Sahalos, "Increased range bistatic scatter radio," *IEEE Trans. Commun.*, vol. 62, no. 3, pp. 1091–1104, Mar. 2014.
- [9] F. Rezaei, C. Tellambura, and S. Herath, "Large-scale wireless-powered networks with backscatter communications—A comprehensive survey," *IEEE open j. Commun. Soc.*, vol. 1, pp. 1100–1130, July 2020.
- [10] G. Yang, C. K. Ho, and Y. L. Guan, "Multi-antenna wireless energy transfer for backscatter communication systems," *IEEE J. Sel. Areas Commun.*, vol. 33, no. 12, pp. 2974–2987, Dec. 2015.
- [11] C. Song *et al.*, "Advances in wirelessly powered backscatter communications: From antenna/RF circuitry design to printed flexible electronics," *Proc. IEEE*, vol. 110, no. 1, pp. 171–192, Jan. 2022.
- [12] P. N. Alevizos *et al.*, "Channel coding for increased range bistatic backscatter radio: Experimental results," in *IEEE RFID Technol. Appl. Conf. (RFID-TA)*, Sep. 2014, pp. 38–43.
- [13] Z. Cui, Z. Wang, G. Wang, R. Xu, and C. Tellambura, "Capacity analysis for tunnel diode amplifier assisted ambient backscatter communications," *IEEE Access*, vol. 10, pp. 98 562–98 571, Sep. 2022.
- [14] X. Jia, X. Zhou, D. Niyato, and J. Zhao, "Intelligent reflecting surface-assisted bistatic backscatter networks: Joint beamforming and reflection design," *IEEE Trans. Green Commun. Netw.*, vol. 6, no. 2, pp. 799–814, Nov. 2022.
- [15] M. Poulakis, "6G's metamaterials solution: There's plenty of bandwidth available if we use reconfigurable intelligent surfaces," *IEEE Spectr.*, vol. 59, no. 11, pp. 40–45, Nov. 2022.
- [16] V. Tapio, I. Hemadeh, A. Mourad, A. Shojaefard, and M. Juntti, "Survey on reconfigurable intelligent surfaces below 10 GHz," *EURASIP J. Wirel. Commun. Netw.*, vol. 2021, no. 1, Sep. 2021.
- [17] P. Nayeri, F. Yang, and A. Elsherbeni, *Reflectarray Antennas: Theory, Designs, and Applications*. Wiley, 2018.
- [18] C. Huang, A. Zappone, G. C. Alexandropoulos, M. Debbah, and C. Yuen, "Reconfigurable intelligent surfaces for energy efficiency in wireless communication," *IEEE Trans. Wireless Commun.*, vol. 18, no. 8, pp. 4157–4170, Aug. 2019.
- [19] E. Björnson, O. Özdogan, and E. G. Larsson, "Reconfigurable intelligent surfaces: Three myths and two critical questions," *IEEE Commun. Mag.*, vol. 58, no. 12, pp. 90–96, Dec. 2020.
- [20] Q. Wu and R. Zhang, "Beamforming optimization for wireless network aided by intelligent reflecting surface with discrete phase shifts," *IEEE Trans. Commun.*, vol. 68, no. 3, pp. 1838–1851, Mar. 2020.
- [21] W. Zhao, G. Wang, S. Atapattu, T. A. Tsiftsis, and X. Ma, "Performance analysis of large intelligent surface aided backscatter communication systems," *IEEE Wireless Commun. Lett.*, vol. 9, no. 7, pp. 962–966, Feb. 2020.
- [22] A. M. T. Khel, K. H. Altuwaigri, and K. A. Hamdi, "Performance analysis of IRS-assisted backscatter communications under hardware imperfections," in *IEEE 95th Veh. Technol. Conf.: (VTC-Spring)*, June 2022, pp. 1–5.
- [23] M. Nemati, J. Ding, and J. Choi, "Short-range ambient backscatter communication using reconfigurable intelligent surfaces," in *IEEE Wireless Commun. Netw. Conf. (WCNC)*, May 2020, pp. 1–6.

- [24] Y. Chen, "Performance of ambient backscatter systems using reconfigurable intelligent surface," *IEEE Commun. Lett.*, vol. 25, no. 8, pp. 2536–2539, May 2021.
- [25] S. Solanki, S. Gautam, S. K. Sharma, and S. Chatzinotas, "Ambient backscatter assisted co-existence in aerial-IRS wireless networks," *IEEE open j. Commun. Soc.*, vol. 3, pp. 608–621, Mar. 2022.
- [26] K. H. Altuwairgi, A. M. T. Khel, and K. A. Hamdi, "Performance analysis of IRS-assisted multi-tag ambient backscatter communications," in *IEEE 95th Veh. Technol. Conf.: (VTC-Spring)*, June 2022, pp. 1–5.
- [27] J. Zuo, Y. Liu, L. Yang, L. Song, and Y.-C. Liang, "Reconfigurable intelligent surface enhanced NOMA assisted backscatter communication system," *IEEE Trans. Veh. Technol.*, vol. 70, no. 7, pp. 7261–7266, June 2021.
- [28] H. Chen, G. Yang, and Y.-C. Liang, "Joint active and passive beamforming for reconfigurable intelligent surface enhanced symbiotic radio system," *IEEE Wireless Commun. Lett.*, vol. 10, no. 5, pp. 1056–1060, Feb. 2021.
- [29] Z. Yang, L. Feng, F. Zhou, X. Qiu, and W. Li, "Analytical performance analysis of intelligent reflecting surface aided ambient backscatter communication network," *IEEE Wireless Commun. Lett.*, vol. 10, no. 12, pp. 2732–2736, Sep. 2021.
- [30] D. Galappaththige, F. Rezaei, C. Tellambura, and S. Herath, "RIS-empowered ambient backscatter communication systems," *IEEE Wireless Commun. Lett.*, vol. 12, no. 1, pp. 173–177, Jan. 2023.
- [31] I. S. Gradshteyn and I. M. Ryzhik, *Table of Integrals, Series, and Products, 7th edition*. Academic Press, 2007.
- [32] Q. Wu and R. Zhang, "Intelligent reflecting surface enhanced wireless network via joint active and passive beamforming," *IEEE Trans. Wireless Commun.*, vol. 18, no. 11, pp. 5394–5409, Nov. 2019.
- [33] R. Long, Y.-C. Liang, H. Guo, G. Yang, and R. Zhang, "Symbiotic radio: A new communication paradigm for passive internet of things," *IEEE Internet Things J.*, vol. 7, no. 2, pp. 1350–1363, 2020.
- [34] D. Galappaththige, D. Kudathanthirige, and G. Amarasuriya, "Performance analysis of distributed intelligent reflective surface aided communications," in *IEEE Global Commun. Conf.*, 2020, pp. 1–6.
- [35] L. Yang, Y. Yang, M. O. Hasna, and M.-S. Alouini, "Coverage, probability of SNR gain, and DOR analysis of RIS-aided communication systems," *IEEE Commun. Lett.*, vol. 9, no. 8, pp. 1268–1272, Aug. 2020.
- [36] S. Ma, Y. Zhu, G. Wang, and R. He, "Machine learning aided channel estimation for ambient backscatter communication systems," in *IEEE Int. Conf. Commun. Syst. (ICCS)*, Dec. 2018, pp. 67–71.
- [37] F. Rezaei, D. Galappaththige, C. Tellambura, and A. Maaref, "Time-spread pilot-based channel estimation for backscatter networks," *arXiv preprint arXiv:2305.17248*, 2023.
- [38] L. Wei *et al.*, "Channel estimation for RIS-empowered multi-user MISO wireless communications," *IEEE Trans. Commun.*, vol. 69, no. 6, pp. 4144–4157, June 2021.
- [39] E. Björnson *et al.*, "Reconfigurable intelligent surfaces: A signal processing perspective with wireless applications," *IEEE Signal Process. Mag.*, vol. 39, no. 2, pp. 135–158, Feb. 2022.
- [40] Q. Tao, Y. Li, C. Zhong, S. Shao, and Z. Zhang, "A novel interference cancellation scheme for bistatic backscatter communication systems," *IEEE Commun. Lett.*, vol. 25, no. 6, pp. 2014–2018, June 2021.
- [41] N. Fasarakis-Hilliard, P. N. Alevizos, and A. Bletsas, "Coherent detection and channel coding for bistatic scatter radio sensor networking," *IEEE Trans. Commun.*, vol. 63, no. 5, pp. 1798–1810, May 2015.
- [42] D. T. Hoang, D. Niyato, D. I. Kim, N. V. Huynh, and S. Gong, *Ambient Backscatter Communication Networks*. Cambridge University Press, 2020.
- [43] Y. Chen and C. Chiu, "Maximum achievable power conversion efficiency obtained through an optimized rectenna structure for RF energy harvesting," *IEEE Trans. Antennas Propag.*, vol. 65, no. 5, pp. 2305–2317, May 2017.
- [44] D. Wang, F. Rezaei, and C. Tellambura, "Performance analysis and resource allocations for a WPCN with a new nonlinear energy harvester model," *IEEE open j. Commun. Soc.*, vol. 1, pp. 1403–1424, Sep. 2020.
- [45] B. Clerckx and E. Bayguzina, "Waveform design for wireless power transfer," *IEEE Trans. Signal Process.*, vol. 64, no. 23, pp. 6313–6328, Dec. 2016.
- [46] A. Collado and A. Georgiadis, "Optimal waveforms for efficient wireless power transmission," *IEEE Microw. Wireless Compon. Lett.*, vol. 24, no. 5, pp. 354–356, Mar. 2014.
- [47] B. Lyu, D. T. Hoang, and Z. Yang, "User cooperation in wireless-powered backscatter communication networks," *IEEE Wireless Commun. Lett.*, vol. 8, no. 2, pp. 632–635, Apr. 2019.
- [48] I. Florescu, *Probability and Stochastic Processes*. Wiley, 2014.
- [49] A. Papoulis and S. U. Pillai, *Probability, random variables, and stochastic processes*. Tata McGraw-Hill Education, 2002.
- [50] Q. Zhang, S. Jin, K.-K. Wong, H. Zhu, and M. Matthaiou, "Power scaling of uplink massive MIMO systems with arbitrary-rank channel means," *IEEE J. Sel. Topics Signal Process.*, vol. 8, no. 5, pp. 966–981, May 2014.
- [51] E. Björnson and L. Sanguinetti, "Power scaling laws and near-field behaviors of massive MIMO and intelligent reflecting surfaces," *IEEE Open J. Commun. Society*, vol. 1, pp. 1306–1324, Sept. 2020.
- [52] J. Proakis, *Digital Communications 5th Edition*. McGraw Hill, 2007.
- [53] Y. Chen and C. Tellambura, "Infinite series representations of the trivariate and quadrivariate Rayleigh distribution and their applications," *IEEE Trans. Commun.*, vol. 53, no. 12, pp. 2092–2101, Dec. 2005.
- [54] C. Tellambura, "Evaluation of the exact union bound for trellis-coded modulations over fading channels," *IEEE Trans. Commun.*, vol. 44, no. 12, pp. 1693–1699, Dec. 1996.
- [55] Z. Wang and G. Giannakis, "A simple and general parameterization quantifying performance in fading channels," *IEEE Trans. Commun.*, vol. 51, no. 8, pp. 1389–1398, Aug. 2003.
- [56] C. Boyer and S. Roy, "Space time coding for backscatter RFID," *IEEE Trans. Wireless Commun.*, vol. 12, no. 5, pp. 2272–2280, May 2013.
- [57] S. Haykin and M. Moher, *Communication Systems*, 5th ed. Wiley India Pvt. Limited, 2009.
- [58] D. Galappaththige and G. Aruma Baduge, "Exploiting distributed IRSs for enabling SWIPT," *IEEE Wireless Commun. Lett.*, vol. 11, no. 4, pp. 673–677, Apr. 2022.
- [59] K. Shen and W. Yu, "Fractional Programming for Communication Systems-Part I: Power Control and Beamforming," *IEEE Trans. Signal Process.*, vol. 66, no. 10, pp. 2616–2630, Mar. 2018.
- [60] S. Boyd and L. Vandenberghe, *Convex Optimization*. Cambridge University Press, March 2004.
- [61] "3GPP TSG RAN –97e3, Study on ambient IoT, 9.1 (from RP-222685)," Sep. 2022. Available Online: <https://portal.3gpp.org/ngppapp/TdocList.aspx?meetingId=60043>.
- [62] A. Ben-Tal and A. S. Nemirovskii, *Lectures on Modern Convex Optimization: Analysis, Algorithms, and Engineering Applications*. USA: Society for Industrial and Applied Mathematics, 2001.
- [63] "3GPP TR 36.814, further advancements for E-UTRA physical layer aspects, V.9.0.0 Rel. 9," Mar. 2010. Available Online: <https://portal.3gpp.org/desktopmodules/Specifications/SpecificationDetails.aspx?specificationId=60043>.
- [64] M. López-Benítez and F. Casadevall, "Versatile, accurate, and analytically tractable approximation for the Gaussian Q-function," *IEEE Trans. Commun.*, vol. 59, no. 4, pp. 917–922, Apr. 2011.